



Master's Thesis

# Global determination of parton distribution functions in the real photon at next-to-leading order in QCD including uncertainties

Alexander Epping  
Universität Münster  
Institute for Theoretical Physics

First Examiner: Prof. Dr. Michael Klasen  
Second Examiner: Priv.-Doz. Dr. Karol Kovařík

Münster, December 12, 2023

# Contents

<b>1. Introduction</b>	<b>1</b>
<b>2. Structure of the Proton in QCD</b>	<b>2</b>
2.1. Quantum Chromodynamics (QCD)	2
2.2. Deep Inelastic Scattering (DIS) on Protons	2
2.3. QCD Corrections	4
<b>3. Parton Distribution Functions in the Real Photon</b>	<b>8</b>
3.1. Introduction	8
3.2. Inhomogeneous DGLAP Equations for Photon DIS	9
3.3. $F_2^\gamma$ Structure Function for Photon DIS	12
3.4. $\text{DIS}_\gamma$ Factorization Scheme	12
3.5. Heavy Quarks	14
<b>4. Numerical Implementation of the Evolution of Photon PDFs using APFEL++</b>	<b>16</b>
4.1. Implementation	16
4.1.1. QCD Evolution Basis	16
4.1.2. Continuation of Implementation	19
4.2. Input	19
4.3. Results	20
<b>5. Fitting of Initial Parameters using <math>\chi^2</math>-Minimization</b>	<b>23</b>
5.1. Input PDFs	23
5.2. Momentum Sum Rule	24
5.3. Implementation	24
5.4. Input	25
5.4.1. Initial Free Parameters	25
5.4.2. Evolution Parameters	26
5.4.3. Used Data on $F_2^\gamma$	26
5.5. Results	27
<b>6. Calculation of Error PDFs</b>	<b>30</b>
6.1. Implementation	30
6.1.1. Hessian Matrix	30
6.1.2. Tolerance $\Delta\chi^2$	31
6.1.3. Error PDF Parameters	33
6.2. Inputs	34
6.3. Results	34

<b>7. Comparison to measured <math>F_2^\gamma</math> and other Photon PDFs</b>	<b>42</b>
7.1. Comparison of Structure Functions . . . . .	42
7.2. Comparison of PDFs . . . . .	45
<b>8. Conclusion and Outlook</b>	<b>48</b>
8.1. Conclusion . . . . .	48
8.2. Outlook . . . . .	48
<b>A. Appendix</b>	<b>49</b>
A.1. Splitting Functions . . . . .	49
A.2. Input PDFs . . . . .	50
A.3. $\chi^2$ Values . . . . .	51
A.4. Error Parameters . . . . .	51
<b>References</b>	<b>53</b>
<b>Acknowledgements</b>	<b>57</b>

## 1. Introduction

Parton distribution functions (PDFs) are commonly used in high-energy physics to describe scattering processes. They describe the probability of a specific parton (i.e. quark or gluon) to have the momentum fraction  $x$  of a hadron, which they are a part of. Since the PDFs are non-perturbative quantities they have to be determined from experimental data. Usually these PDFs are calculated for an initial energy scale using data from deep inelastic scattering experiments where a virtual photon collides with a proton or nucleus. Using the Dokshitzer-Gribov-Lipatov-Altarelli-Parisi (DGLAP) evolution equations these PDFs can then be evolved to higher energy scales.

For proton and nuclei the DGLAP equations are homogeneous differential equations. For the deep inelastic scattering of a virtual with a real photon (i.e. for photon PDFs) they become inhomogeneous. The reason for that is that the real photon does not only behave hadron-like, i.e. similar to for example a proton, but also interacts with/fluctuates into quark-antiquark pairs. This is called the point-like contribution which is responsible for the inhomogeneous part of the DGLAP evolution equations.

The photon PDFs have already been extracted in previous literature, however there were always some shortcomings.

This thesis aims to improve on that by calculating the photon PDFs using a modified version of the evolution library **APFEL++** written in C++ [1, 2], which is a more modern evolution library than used in previous publications. Furthermore the calculated photon PDFs will not violate the momentum sum rule and include new research data. Most importantly the uncertainties of the photon PDFs (i.e. error PDFs) will be calculated and the methods used for their calculation will be provided.

This thesis is structured as follows:

**Chapter 2:** This chapter gives a short theoretical overview on QCD, deep inelastic scattering of the proton and the associated DGLAP equations.

**Chapter 3:** Building upon the previous chapter the theory describing the deep inelastic scattering of real photons is given.

**Chapter 4:** Next the implementation of the inhomogeneous DGLAP evolution equation into **APFEL++** is explained.

**Chapter 5:** In this chapter it is shown how the fitting of the free initial parameters to the available  $F_2^\gamma$  data is done by minimizing the  $\chi^2$  using **MINUIT**.

**Chapter 6:** Here the calculation of error PDFs using the Hessian method is explained.

**Chapter 7:** The results of the previous chapters are presented and the calculated PDFs and  $F_2^\gamma$  structure functions are compared to previous photon PDFs and the experimental data respectively.

## 2. Structure of the Proton in QCD

Unless stated otherwise, sections 2.2 and 2.3 follow the theoretical parts of [3, 4] closely. For further details please refer to these sources.

### 2.1. Quantum Chromodynamics (QCD)

The theory of strong interactions is called quantum chromodynamics (QCD). It explains the interactions between hadrons and also the particles they are made of. These particles, gluons and quarks, are called partons. One of the most prominent tools to analyse these interactions is pQCD, where the result is approximated by expressing it as a power series. This can be done because of the asymptotic freedom which is, next to the confinement, one of the main features of QCD. The asymptotic freedom states that with large enough momentum ( $Q^2 \gg 1 \text{ GeV}^2$ ) or probed distances smaller than the size of the probed hadron, the interaction strength, i.e. the strong coupling constant  $\alpha_s(Q^2)$ , becomes weaker.

When the goal is to observe the distribution of partons inside a hadron, deep inelastic scattering (DIS) is used on the experimental side to gather data. Since the description of the distribution however should be independent of the process, factorization is used to split the description of the experimental results into two parts. One of these parts, the parton distribution functions (PDFs), are process-independent, meaning they universally describe the partonic structure/distribution of the probed hadron [4].

### 2.2. Deep Inelastic Scattering (DIS) on Protons

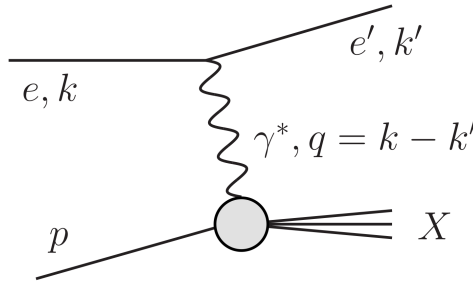


**Figure 1:** Electron - Proton DIS. [3]

If the momentum transfer squared  $Q^2 = -q^2$  of the virtual photon during  $e + p \rightarrow e' + X$  processes (see fig. 1) becomes large enough, the (target) proton does not scatter elastically, but inelastically. This means that now the proton does not behave like a point-like particle anymore, but rather as a particle made up of structureless partons.

## 2. Structure of the Proton in QCD

---

The inelastic electron - proton scattering can be seen as an elastic scattering of the electron and a 'free' quark within the proton. This means that large  $Q^2$  virtual photons resolve the 'point' constituents of the proton [5].

The scattering amplitude of such a process is given by

$$\mathcal{M} = \frac{4\pi\alpha}{q^2} \bar{u}(k') \gamma^\mu u(k) \langle X | J_\mu(0) | p \rangle, \quad (2.1)$$

with the electromagnetic fine-structure constant  $\alpha = e^2/4\pi$  and the matrix element  $\langle X | J_\mu(0) | p \rangle$  of the current  $J_\mu$  between the initial proton and the final  $X$  states. The variable  $x = \frac{Q^2}{2(p \cdot q)}$  is the fraction of the momentum of the proton carried by the parton interacting with the virtual photon.

The cross section then reads

$$d\sigma = \frac{16\pi^3 \alpha^2 M}{q^4 (k \cdot p)} L^{\mu\nu} W_{\mu\nu} \frac{d^3 \vec{k}'}{2E_{k'} (2\pi)^3}, \quad (2.2)$$

where  $L^{\mu\nu}$  stands for the leptonic tensor

$$L^{\mu\nu} = \frac{1}{2} \sum_{\text{pol}} \bar{u}(k) \gamma^\nu u(k') \bar{u}(k') \gamma^\mu u(k) = 2(k'^\mu k^\nu + k'^\nu k^\mu - g^{\mu\nu} (k' \cdot k)) \quad (2.3)$$

and  $W_{\mu\nu}$  for the hadronic tensor

$$\begin{aligned} W_{\mu\nu} &= \frac{1}{4\pi M} \frac{1}{2} \sum_{\text{pol}} \sum_X (2\pi)^4 \delta^4(k + p - k' - p_X) \langle p | J_\nu(0) | X \rangle \langle X | J_\mu(0) | p \rangle \frac{d^3 p_X}{2E_{p_X} (2\pi)^3} \\ &= -\frac{F_1}{M} \left( g_{\mu\nu} - \frac{q_\mu q_\nu}{q^2} \right) + \frac{F_2}{\nu M^2} \left( p_\mu - \frac{(p \cdot q)}{q^2} q_\mu \right) \left( p_\nu - \frac{(p \cdot q)}{q^2} q_\nu \right). \end{aligned} \quad (2.4)$$

The hadronic tensor can be expressed in terms of the structure functions  $F_1$  and  $F_2$  with

$$\begin{aligned} F_1 &= \left( -\frac{1}{2} g^{\mu\nu} + \frac{2x^2}{Q^2} p^\mu p^\nu \right) M W_{\mu\nu} \\ \frac{F_2}{x} &= \left( -g^{\mu\nu} + \frac{12x^2}{Q^2} p^\mu p^\nu \right) M W_{\mu\nu}. \end{aligned} \quad (2.5)$$

This leads to the DIS cross section

$$\frac{d\sigma}{dx dQ^2} = \frac{4\pi\alpha^2}{Q^4} \frac{1}{x} \left( xy^2 F_1 + F_2 \left( 1 - y - \frac{x^2 y^2 M^2}{Q^2} \right) \right) \quad (2.6)$$

with  $y = \frac{(p \cdot q)}{(p \cdot k)}$ .

For the so called quark parton model, i.e. electron - proton DIS without gluon emission and loops, one receives as expressions for the structure functions

$$\begin{aligned} F_1(x) &= \frac{1}{2} \sum_q e_q^2 f_q(x) \\ F_2(x) &= \sum_q e_q^2 x f_q(x), \end{aligned} \quad (2.7)$$

where  $f_q(x)$  is the density of the quark  $q$  in the proton.

Together with eq. (2.6) this leads to the cross section for DIS in the quark parton model

$$\frac{d\sigma}{dx dQ^2} = \frac{4\pi\alpha^2}{Q^4} \left( \frac{y^2}{2} - \left( 1 - y - \frac{x^2 y^2 M^2}{Q^2} \right) \right) \sum_q e_q^2 f_q(x) = \frac{d\hat{\sigma}_0}{dx dQ^2} \sum_q e_q^2 f_q(x), \quad (2.8)$$

with the partonic Born cross section

$$\frac{d\hat{\sigma}_0}{dx dQ^2} = \frac{4\pi\alpha^2}{Q^4} \left( \frac{y^2}{2} - \left( 1 - y - \frac{x^2 y^2 M^2}{Q^2} \right) \right). \quad (2.9)$$

### 2.3. QCD Corrections

As already mentioned the parton model does not show the whole picture. There are still two types of QCD corrections to the DIS cross section to consider:

- real gluon and quark emission off quark and gluon legs
- virtual corrections, i.e. loop corrections to quark and gluon propagators and quark-gluon vertices

These calculations in pQCD are simplified by using the axial gauge for the gluon propagator.

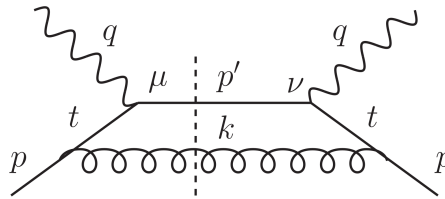


**Figure 2:** Real gluon emission off incoming quark (quark-initiated parton ladder) in cut diagram notation. [3]

## 2. Structure of the Proton in QCD

---

The main contributor to the corrections is the emission of a real gluon off the incoming quark. This is shown in fig. 2. The corresponding hadronic tensor can be calculated as

$$-g^{\mu\nu} MW_{\mu\nu} = \sum_q e_q^2 \frac{\alpha_s}{2\pi} \ln \left( \frac{Q^2}{m^2} \right) \int_x^1 \frac{dz}{z} P_{qq}(z) f_q \left( \frac{x}{z} \right) \quad (2.10)$$

in the leading logarithmic approximation (LLA), where the  $m^2$  was introduced as an arbitrary cutoff and  $P_{qq}(z) = C_F \frac{1+z^2}{1-z}$  is the quark-quark splitting function with  $C_F = 4/3$ .

Combining eq. (2.10) with the result for the parton model at leading-order, eq. (2.8), results in the DIS cross section in LLA:

$$\frac{d\sigma}{dx dQ^2} = \frac{d\hat{\sigma}_0}{dx dQ^2} \sum_q e_q^2 \left( 1 + \frac{\alpha_s}{2\pi} \ln \left( \frac{Q^2}{m^2} \right) P_{qq} \right) \otimes f_q, \quad (2.11)$$

with the convolution  $\otimes$  defined as

$$\begin{aligned} 1 \otimes f_q &\equiv \int_x^1 \frac{dz}{z} \delta(z-1) f_q \left( \frac{x}{z} \right) = f_q(x) \\ P_{qq} \otimes f_q &\equiv \int_x^1 \frac{dz}{z} P_{qq}(z) f_q \left( \frac{x}{z} \right). \end{aligned} \quad (2.12)$$

By adding more gluon 'steps' to the ladder, the cross section becomes

$$\frac{d\sigma}{dx dQ^2} = \frac{d\hat{\sigma}_0}{dx dQ^2} \sum_q e_q^2 \exp \left[ \frac{\alpha_s}{2\pi} \ln \left( \frac{Q^2}{m^2} \right) P_{qq} \right] \otimes f_q \quad (2.13)$$

with the convolution

$$P_{qq} \otimes P_{qq} \otimes f_q \equiv \int_x^1 \frac{dz'}{z'} P_{qq}(z') \int_{x/z'}^1 \frac{dz}{z} P_{qq}(z) f_q \left( \frac{x}{zz'} \right). \quad (2.14)$$

For the gluon-initiated parton ladder (see fig. 3) the contribution to the DIS cross section in LLA is

$$\frac{d\sigma}{dx dQ^2} = \frac{d\hat{\sigma}_0}{dx dQ^2} \sum_q e_q^2 \frac{\alpha_s}{2\pi} \ln \left( \frac{Q^2}{m^2} \right) P_{qg} \otimes f_g \quad (2.15)$$

with the quark-gluon splitting function  $P_{qg}(z) = T_R (z^2 + (1-z)^2)$  where  $T_R = 1/2$ .



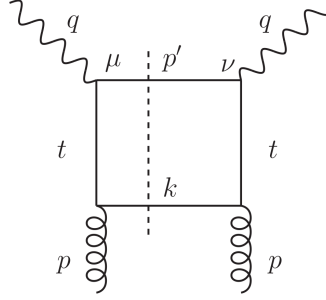


**Figure 3:** Gluon-initiated parton ladder in cut diagram notation. [3]

Including more quark 'steps', all corrections so far can be combined and are equivalent to replacing the  $Q^2$ -independent  $f_i(x)$  with the to the parton distribution functions (PDF)  $f_i(x, Q^2)$  for the quark and gluon

$$\begin{pmatrix} f_q(x) \\ f_g(x) \end{pmatrix} \rightarrow \begin{pmatrix} f_q(x, Q^2) \\ f_g(x, Q^2) \end{pmatrix} = \exp \left[ \frac{\alpha_s}{2\pi} \ln \left( \frac{Q^2}{m^2} \right) \begin{pmatrix} P_{qq} & P_{qg} \\ P_{gq} & P_{gg} \end{pmatrix} \right] \otimes \begin{pmatrix} f_q \\ f_g \end{pmatrix} \quad (2.16)$$

in the result for the parton model, eq. (2.8). From eq. (2.16) one obtains the famous Dokshitzer-Gribov-Lipatov-Altarelli-Parisi (DGLAP) evolution equation

$$Q^2 \frac{\partial}{\partial Q^2} \begin{pmatrix} f_q(x, Q^2) \\ f_g(x, Q^2) \end{pmatrix} = \frac{\alpha_s}{2\pi} \begin{pmatrix} P_{qq} & P_{qg} \\ P_{gq} & P_{gg} \end{pmatrix} \otimes \begin{pmatrix} f_q(Q^2) \\ f_g(Q^2) \end{pmatrix}, \quad (2.17)$$

describing the higher-order corrections to the parton model predictions.

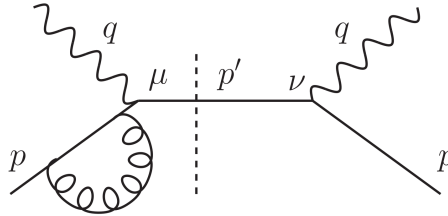


**Figure 4:** Virtual correction to quark-initiated parton ladder. [3]

The virtual corrections (see fig. 4) lead to a DIS cross section in LLA, including quark contributions, of

$$\begin{aligned} \frac{d\sigma}{dx dQ^2} &= \frac{d\hat{\sigma}_0}{dx dQ^2} \sum_q e_q^2 \left( Z_q(-m^2) + \frac{\alpha_s}{2\pi} \ln \left( \frac{Q^2}{m^2} \right) P_{qq} \right) \otimes f_q \\ &= \frac{d\hat{\sigma}_0}{dx dQ^2} \sum_q e_q^2 \left( Z_q(-Q^2) + \frac{\alpha_s}{2\pi} \ln \left( \frac{Q^2}{m^2} \right) \tilde{P}_{qq} \right) \otimes f_q \end{aligned}$$

with

$$Z_q(-Q^2) = 1 - \frac{\alpha_s}{2\pi} C_F \ln \left( \frac{\Lambda^2}{Q^2} \right) \int_0^1 dz \frac{1+z^2}{1-z} \quad (2.18)$$

and the plus-prescription of the quark-quark splitting function

$$\tilde{P}_{qq}(z) = C_F \left( \frac{1+z^2}{1-z} \right)_+ \quad (2.19)$$

with

$$\left( \frac{1+z^2}{1-z} \right)_+ \equiv \left( \frac{1+z^2}{1-z} \right) - \delta(1-z) \int_0^1 dz' \left( \frac{1+z'^2}{1-z'} \right). \quad (2.20)$$

The plus-prescription does not have the  $z = 1$  singularity meaning it is canceled by the virtual corrections.

Eq. (2.18) can be compared to eq. (2.11), where the only difference are the missing virtual corrections.

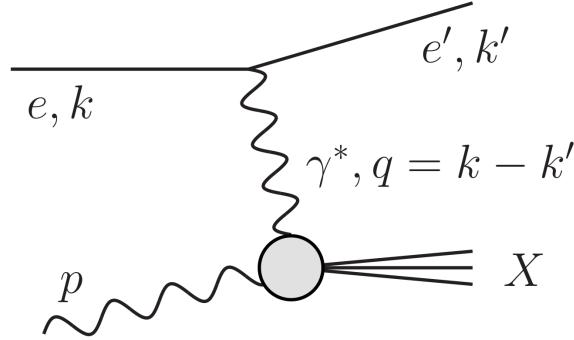


**Figure 5:** Electron - photon DIS. [3]

### 3. Parton Distribution Functions in the Real Photon

The discussion of the theory follows [3, 6] closely, unless stated otherwise. For further information please refer to these references and [7, 8, 9].

#### 3.1. Introduction

The photon, as a boson, plays a dual role in strong interactions. It can interact directly with charged particles aswell as indirectly through particles created by fluctuating into a charged fermion antifermion pair. This pair carries the same quantum numbers as the photon. The photon is called *resolved* during the indirect interactions, whereas it is called *direct* or *bare* in the first case. The different interactions of the photon can be seen in fig. 6.

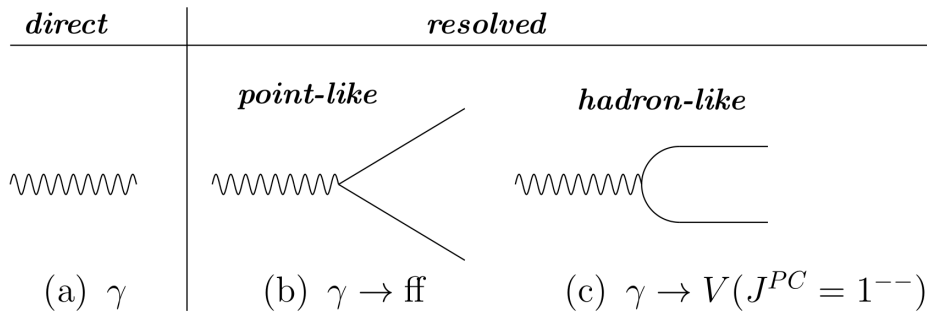


**Figure 6:** The different appearances of the photon. Shown are (a) the direct or bare photon, and (b,c) the resolved photon, which can be either point-like, (b), or hadron-like, (c) [6, Fig. 2].

For the calculation of photon PDFs during DIS on a real photon (see fig. 5) the direct

interaction with particles is not of interest since it does not reveal the structure of the photon. Interactions with the resolved photon however reveal it's structure.

As illustrated in fig. 6 the resolved photon appears in two distinguishable forms. The point-like and the hadron-like (or also called hadronic).

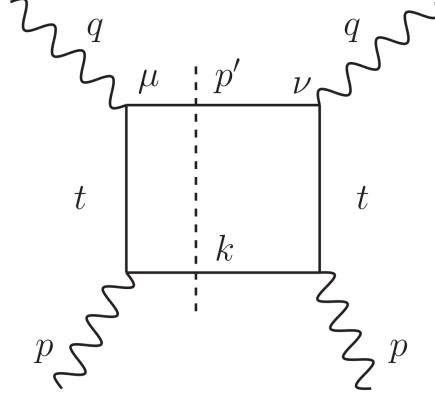


**Figure 7:** Quark box diagram in cut diagram notation. [3]

The point-like part, where the photon splits into a quark antiquark pair, leads to the interaction shown in the so called quark box diagram fig. 7. This part can be calculated perturbatively and is represented by the inhomogeneous part of the DGLAP evolution equations for the photon.

On the other hand the hadron-like part appears if the photon, as the name suggests, fluctuates into a hadronic state. This part can not be calculated perturbatively.

### 3.2. Inhomogeneous DGLAP Equations for Photon DIS

The DGLAP eqvolution equations for the photon DIS are given by

$$\begin{aligned}
 \frac{dq_i^\gamma}{d \ln Q^2} &= \frac{\alpha}{2\pi} P_{q_i \gamma} \otimes \Gamma^\gamma + \frac{\alpha_s}{2\pi} \left\{ \sum_{k=1}^f [P_{q_i q_k} \otimes q_k^\gamma + P_{q_i \bar{q}_k} \otimes \bar{q}_k^\gamma] + P_{q_i g} \otimes g^\gamma \right\} \\
 \frac{d\bar{q}_i^\gamma}{d \ln Q^2} &= \frac{\alpha}{2\pi} P_{\bar{q}_i \gamma} \otimes \Gamma^\gamma + \frac{\alpha_s}{2\pi} \left\{ \sum_{k=1}^f [P_{\bar{q}_i q_k} \otimes q_k^\gamma + P_{\bar{q}_i \bar{q}_k} \otimes \bar{q}_k^\gamma] + P_{\bar{q}_i g} \otimes g^\gamma \right\} \\
 \frac{dg^\gamma}{d \ln Q^2} &= \frac{\alpha}{2\pi} P_{g \gamma} \otimes \Gamma^\gamma + \frac{\alpha_s}{2\pi} \left\{ \sum_{k=1}^f [P_{g q_k} \otimes q_k^\gamma + P_{g \bar{q}_k} \otimes \bar{q}_k^\gamma] + P_{g g} \otimes g^\gamma \right\} \\
 \frac{d\Gamma^\gamma}{d \ln Q^2} &= \frac{\alpha}{2\pi} P_{\gamma \gamma} \otimes \Gamma^\gamma + \frac{\alpha}{2\pi} \left\{ \sum_{k=1}^f [P_{\gamma q_k} \otimes q_k^\gamma + P_{\gamma \bar{q}_k} \otimes \bar{q}_k^\gamma] + P_{\gamma g} \otimes g^\gamma \right\},
 \end{aligned} \tag{3.1}$$

### 3. Parton Distribution Functions in the Real Photon

---

where the parton distributions for the quarks and antiquarks are  $q_i^\gamma(x, Q^2)$  and  $\bar{q}_i^\gamma(x, Q^2)$ , the gluon distribution is  $g^\gamma(x, Q^2)$  and the photon distribution  $\Gamma^\gamma(x, Q^2)$ . The  $P_{ab}$  are the usual splitting functions. They are illustrated in fig. 24.  $n_f$  refers to the number of active quark flavours, i.e. the number of quark flavours which can be produced at the given  $Q^2$ .

For the case of the photon  $q_i^\gamma = \bar{q}_i^\gamma$ .

Because the QED coupling constant  $\alpha \approx 1/137 \ll 1$  it is sufficient to expand eq. (3.1) only up to  $\mathcal{O}(\alpha)$ . This means that  $P_{\gamma q_k}$ ,  $P_{\gamma \bar{q}_k}$  and  $P_{\gamma g}$  do not contribute and since photon radiation starts at  $\alpha^2$  one can use

$$P_{\gamma\gamma} \propto \delta(1-x) \quad (3.2)$$

for all orders in  $\alpha_s$ . The photon distribution function can now be calculated explicitly as

$$\Gamma_{\text{LO}}^\gamma(x, Q^2) = \delta(1-x) \left[ 1 - \frac{\alpha}{\pi} \left( \sum_{k=1}^{n_f} e_{q_k}^2 \ln \left( \frac{Q^2}{Q_0^2} + c_1 \right) \right) \right], \quad (3.3)$$

where  $Q_0^2$  is the starting scale of the evolution and  $c_1$  is an unknown parameter.

To keep the distribution functions at  $\mathcal{O}(\alpha)$ , only the  $\mathcal{O}(\alpha^0)$  contribution of  $\Gamma^\gamma$  will be used, resulting in

$$\begin{aligned} \frac{dq_i^\gamma}{d \ln Q^2} &= \frac{\alpha}{2\pi} P_{q_i\gamma} + \frac{\alpha_s}{2\pi} \left\{ \sum_{k=1}^f [P_{q_i q_k} + P_{q_i \bar{q}_k}] \otimes q_k^\gamma + P_{q_i g} \otimes g^\gamma \right\} \\ \frac{dg^\gamma}{d \ln Q^2} &= \frac{\alpha}{2\pi} P_{g\gamma} + \frac{\alpha_s}{2\pi} \left\{ \sum_{k=1}^f [P_{g q_k} + P_{g \bar{q}_k}] \otimes q_k^\gamma + P_{gg} \otimes g^\gamma \right\}. \end{aligned} \quad (3.4)$$

Rewriting these equations in terms of the non-singlet and singlet quark and perturbatively expanding the splitting functions in  $\alpha_s$  one receives

$$\begin{aligned} \frac{dq_{NS}^\gamma(x, Q^2)}{d \ln Q^2} &= \frac{\alpha}{2\pi} \left( k_{NS}^{(0)}(x) + \frac{\alpha_s}{2\pi} k_{NS}^{(1)}(x) \right) + \frac{\alpha_s}{2\pi} \left( P_{qq}^{(0)} + \frac{\alpha_s}{2\pi} P_{qq}^{(1)} \right) \otimes q_{NS}^\gamma \\ \frac{d\Sigma^\gamma(x, Q^2)}{d \ln Q^2} &= \frac{\alpha}{2\pi} \left( k_q^{(0)}(x) + \frac{\alpha_s}{2\pi} k_q^{(1)}(x) \right) + \frac{\alpha_s}{2\pi} \left( P_{qq}^{(0)} + \frac{\alpha_s}{2\pi} P_{qq}^{(1)} \right) \otimes \Sigma^\gamma \\ &\quad + \frac{\alpha_s}{2\pi} \left( P_{qg}^{(0)} + \frac{\alpha_s}{2\pi} P_{qg}^{(1)} \right) \otimes g^\gamma \\ \frac{dg^\gamma(x, Q^2)}{d \ln Q^2} &= \frac{\alpha}{2\pi} \frac{\alpha_s}{2\pi} k_g^{(1)}(x) + \frac{\alpha_s}{2\pi} \left( P_{gg}^{(0)} + \frac{\alpha_s}{2\pi} P_{gg}^{(1)} \right) \otimes \Sigma^\gamma \\ &\quad + \frac{\alpha_s}{2\pi} \left( P_{gg}^{(0)} + \frac{\alpha_s}{2\pi} P_{gg}^{(1)} \right) \otimes g^\gamma, \end{aligned} \quad (3.5)$$

where the quark non-singlet is

$$q_{NS}^\gamma(x, Q^1) = \sum_{q=1}^{n_f} (e_q^2 - \langle e^2 \rangle) (q^\gamma(x, Q^2) + \bar{q}^\gamma(x, Q^2)) \quad (3.6)$$

and the quark singlet

$$\Sigma^\gamma(x, Q^2) = \sum_{q=1}^{n_f} (q^\gamma(x, Q) + \bar{q}^\gamma(x, Q^2)). \quad (3.7)$$

Here

$$\langle e^i \rangle = \frac{1}{n_f} \sum_{q=1}^{n_f} e_i^2 \quad (3.8)$$

was used.

The splitting functions  $P_{ij}^{(0,1)}$  are the same as in the proton case and can be seen in eq. (A.1). The splitting functions stemming from the point-like coupling, i.e. the quark box diagram, can be calculated from the splitting functions in eq. (3.4) and are given by [7, 8]

$$\begin{aligned} k_{NS}^{(0)} &= 3n_f (\langle e^4 \rangle - (\langle e^2 \rangle)^2) 2(x^2 + (1-x)^2) \\ k_{NS}^{(1)} &= 3n_f (\langle e^4 \rangle - (\langle e^2 \rangle)^2) k(x) \\ k_q^{(0)} &= 3n_f \langle e^2 \rangle 2(x^2 + (1-x)^2) \\ k_q^{(1)} &= 3n_f \langle e^2 \rangle k(x) \\ k_g^{(1)} &= 3n_f \langle e^2 \rangle \frac{4}{3} \left[ -16 + 8x + \frac{20}{3}x^2 + \frac{4}{3x} - (6 + 10x) \ln(x) - 2(1+x)(\ln(x))^2 \right] \end{aligned} \quad (3.9)$$

with

$$\begin{aligned} k(x) &= \frac{4}{3} \left[ 4 - 9x - (1-4x) \ln(x) - (1-2x)(\ln(x))^2 + 4 \ln(1-x) \right. \\ &\quad + (4 \ln(x) - 4 \ln(x) \ln(1-x) + 2(\ln(x))^2 - 4 \ln(1-x) + 2(\ln(1-x))^2 \\ &\quad \left. - \frac{2}{3}\pi^2 + 10)(x^2 + (1-x)^2) \right]. \end{aligned} \quad (3.10)$$

The DGLAP evolution equations for the photon, eq. (3.5), are inhomogeneous because of the point-like couplings, i.e. the coupling of photons to quarks. Without this coupling the evolution equations would be homogeneous and the same as for the proton. Because of this the homogeneous solution of eq. (3.5) is called the hadronic solution and the particular solution the point-like. The general solution of the inhomogeneous DGLAP equations is given by the sum of the two solutions

$$\begin{aligned} q^\gamma(x, Q^2) &= q_{pl}^\gamma(x, Q^2) + q_{had}^\gamma(x, Q^2) \\ g^\gamma(x, Q^2) &= g_{pl}^\gamma(x, Q^2) + g_{had}^\gamma(x, Q^2). \end{aligned} \quad (3.11)$$

### 3.3. $F_2^\gamma$ Structure Function for Photon DIS

The contribution of the quark box diagram, i.e. the point-like contribution, to the  $F_2^\gamma$  structure function is given by [3]

$$\frac{F_2^\gamma(x, Q^2)}{x} = \frac{\alpha}{2\pi} 2 \sum_f e_f^4 N_c \left[ (x^2 + (1-x)^2) \ln \left( \frac{1-x}{x} \right) - 1 + 8x(1-x) \right]. \quad (3.12)$$

In the so called  $\overline{\text{MS}}$  factorization scheme (see section 3.4) at NLO the complete  $F_2^\gamma(x, Q^2)$  structure function reads [3, 7, 8]

$$\begin{aligned} \frac{F_2^\gamma(x, Q^2)}{x} = & \left( 1 + \frac{\alpha_s(Q^2)}{4\pi} B_q \right) \otimes q_{NS}^\gamma + \langle e^2 \rangle \left( 1 + \frac{\alpha_s(Q^2)}{4\pi} B_q \right) \otimes \Sigma^\gamma \\ & + \langle e^2 \rangle \frac{\alpha_s(Q^2)}{4\pi} B_g \otimes g^\gamma + 3n_f \langle e^4 \rangle \frac{\alpha}{4\pi} B_\gamma(x), \end{aligned} \quad (3.13)$$

where  $B_q$  and  $B_g$  are standard NLO coefficient functions

$$B_q(x) = \frac{8}{3} \left[ \frac{9+5x}{4} - \frac{1+x^2}{1-x} \ln x - \frac{3}{4} \frac{1+x^2}{(1-x)_+} + (1+x^2) \left( \frac{\ln(1-x)}{1-x} \right)_+ - \left( \frac{9}{2} + \frac{\pi^2}{3} \right) \delta(1-x) \right] \quad (3.14)$$

$$B_g(x) = 2n_f \left[ (x^2 + (1-x)^2) \ln \left( \frac{1-x}{x} \right) - 1 + 8x(1-x) \right]. \quad (3.15)$$

The photon coefficient function  $B_\gamma(x)$ , representing the point-like contribution to the structure function, is

$$B_\gamma(x) = \frac{2}{n_f} B_g(x). \quad (3.16)$$

In eq. (3.13) the  $B_\gamma(x)$  will lead to numerical instabilities. The reason for that is the  $\ln(1-x)/x$  term in eq. (3.16) which becomes large and negative for  $x \rightarrow 1$ . This however can be avoided by using the  $\text{DIS}_\gamma$  factorization scheme proposed in [8].

### 3.4. $\text{DIS}_\gamma$ Factorization Scheme

In general cross sections for processes with hadrons in the initial state show a combination of short- and long-distance behaviour, which means that they are not directly computable in pQCD. The cross section for DIS on a real photon shows the same behaviour.

The factorization theorems allow to derive predictions for these cross sections by separating (factorizing) the long-distance (non-perturbative) behaviour from the short-distance (perturbative) behaviour in a systematic fashion [10].

### 3. Parton Distribution Functions in the Real Photon

---

For  $F_2(x, Q^2)$  structure functions the factorization leads to [11]

$$F_2(x, Q^2) = \sum_{i=q, \bar{q}, g} \int_x^1 d\xi C_i \left( \frac{x}{\xi}, \frac{Q^2}{\mu^2}, \frac{\mu_f^2}{\mu^2}, \alpha_s(\mu^2) \right) f_i(\xi, \mu_f^2, \mu^2) \quad (3.17)$$

where  $i$  is the parton flavour,  $C_i$  are called coefficient functions (they are the same as  $B_i$ ) and  $f_i$  are parton distributions.  $\mu$  is the renormalization scale appearing in any perturbative calculations [5] ( $\mu^2 = m^2$  is used here), while  $\mu_f$  is the factorization scale separating the perturbative and non-perturbative effects. It is often chosen that  $\mu_f = \mu$ . The short-distance behaviour is described by the coefficient functions  $C_i$ , which are target independent and can be calculated using perturbation theory.

The long-distance behaviour on the other hand is given by the parton distributions  $f_i$  which only depend on the target and not on the process.

To calculate these coefficient functions and parton distributions one needs a prescription for separating the two. This prescription, involving a degree of choice, is called a factorization scheme. One of the most commonly used factorization schemes is called the modified minimal subtraction,  $\overline{\text{MS}}$ , factorization scheme.

For the calculation of  $C_i$  and  $f_i$  in this scheme, each involved quantity is written as a power series of  $\alpha_s$  as indicated by the superscript

$$\begin{aligned} f_i &= f_i^{(0)} + f_i^{(1)} + \dots \\ C_i &= C_i^{(0)} + C_i^{(1)} + \dots \\ F_{2,i} &= C_i^{(0)} \otimes f_i^{(0)} + C_i^{(0)} \otimes f_i^{(1)} + C_i^{(1)} \otimes f_i^{(0)} + \dots \end{aligned} \quad (3.18)$$

For the example of DIS on a quark target for  $\mathcal{O}(\alpha_s^0)$ , i.e. without interactions, the parton distribution is

$$f_i^{(0)}(\xi) = \delta(1 - \xi) \quad (3.19)$$

and since  $F_{2,i}(x) = e_q^2 \delta(1 - x)$  this results in

$$C_q^{(0)}(x) = e_q^2 \delta(1 - x). \quad (3.20)$$

To one-loop accuracy, i.e. for  $\mathcal{O}(\alpha_s)$ , the coefficient functions and parton distributions can be calculated by comparing the  $F_2(x, Q^2)$  structure functions, the DGLAP evolution equations and eqs. (3.17) and (3.18). Using this approach one will be able to derive the standard coefficient functions and splitting functions. This is described in detail in [11]. Please refer there and to [10] for further information on factorization.

The splitting functions, PDFs and coefficient functions given so far are given in this scheme.



The factorization scheme commonly used for the calculation of photon PDFs is called  $\text{DIS}_\gamma$ . It is defined such that the point-like contribution to the  $F_2^\gamma(x, Q^2)$  structure functions is absorbed in the quark distribution. This avoids the aforementioned numerical instabilities at large  $x$ .

The PDFs can be changed from the  $\overline{\text{MS}}$  to the  $\text{DIS}_\gamma$  factorization scheme using

$$\begin{aligned} (q^\gamma(x) + \bar{q}^\gamma(x))_{\text{DIS}_\gamma} &= (q^\gamma(x) + \bar{q}^\gamma(x))_{\overline{\text{MS}}} + e_q^2 \frac{3\alpha}{4\pi} B_\gamma(x) \\ g^\gamma(x)_{\text{DIS}_\gamma} &= g^\gamma(x)_{\overline{\text{MS}}}. \end{aligned} \quad (3.21)$$

The point-like splitting functions at NLO in  $\text{DIS}_\gamma$  are given by

$$\begin{aligned} k_{NS}^{(1)}(x)_{\text{DIS}_\gamma} &= k_{NS}^{(1)}(x)_{\overline{\text{MS}}} - \frac{3n_f}{2} (\langle e^4 \rangle - \langle e^2 \rangle^2) P_{qq}^{(0)} \otimes B_\gamma \\ k_q^{(1)}(x)_{\text{DIS}_\gamma} &= k_q^{(1)}(x)_{\overline{\text{MS}}} - \frac{3n_f}{2} \langle e^2 \rangle P_{qq}^{(0)} \otimes B_\gamma \\ k_g^{(1)}(x)_{\text{DIS}_\gamma} &= k_g^{(1)}(x)_{\overline{\text{MS}}} - \frac{3n_f}{2} \langle e^2 \rangle P_{gq}^{(0)} \otimes B_\gamma. \end{aligned} \quad (3.22)$$

As already mentioned, in the  $\text{DIS}_\gamma$  scheme, the  $F_2^\gamma(x, Q^2)$  structure function at NLO does not contain the  $B_\gamma$  term anymore, which led to the numerical instabilities at large  $x$ . Neglecting higher-order terms the structure function is now given by

$$\frac{F_2^\gamma(x, Q^2)}{x} = \left(1 + \frac{\alpha_s(Q^2)}{4\pi} B_q\right) \otimes q_{NS}^\gamma + \langle e^2 \rangle \left(1 + \frac{\alpha_s(Q^2)}{4\pi} B_q\right) \otimes \Sigma^\gamma + \langle e^2 \rangle \frac{\alpha_s(Q^2)}{4\pi} B_g \otimes g^\gamma. \quad (3.23)$$

This is the same expression as for the proton case.

### 3.5. Heavy Quarks

At low energy scales not every quark flavour is available. This means that by moving to higher  $Q^2$  during the evolution the number of flavours  $n_f$  changes. The unavailable quark flavours are called heavy quarks and when their so called heavy quark threshold (corresponding with the quark mass) is crossed they become available. The way this is handled is referred to as a heavy quark scheme.

One way to handle the heavy quarks is called the zero-mass variable flavour number scheme (ZM-VFNS), where all quarks are treated as massless partons. Furthermore the PDFs of the heavy quarks (quarks with thresholds below the current  $Q^2$ ) are zero. By crossing a quark threshold,  $n_f$  is increased by one and the PDFs of the corresponding quark can be non-zero. This also means that different evolution equations have to be solved for below and above these thresholds and connected using matching conditions at the threshold [1, 3].

The program used for this thesis, **APFEL++**, handles the heavy quarks and matching conditions on its own. Therefore the heavy quarks do not affect the theory discussed so far.

Opposite to the VFNS is the fixed flavour number scheme (FFNS) where, as the name suggests, the number of flavours stays fixed. It is common to choose  $n_f = 3$  and  $u$ ,  $d$  and  $c$  are therefore treated as massless [3].

For more details on ZM-VFNS and FFNS please refer to [12].

The two different heavy quark schemes both have their use cases. FFNS is known to be better for low  $Q^2$  values while ZM-VFNS should be used at high  $Q^2$ . Therefore a combination of the two could result in an improvement over the whole  $Q^2$  range [12].

## 4. Numerical Implementation of the Evolution of Photon PDFs using APFEL++

For the evolution a program called APFEL++ [13] will be used. This program can, amongst other things, evolve PDFs and calculate structure functions. APFEL++ however was originally written with proton and neutron PDFs in mind, which means that the code has to be modified to be able to evolve photon PDFs.

### 4.1. Implementation

As APFEL++ is originally meant for proton and neutron PDFs, it calculates the results of homogeneous differential equations (DEs), i.e.

$$\frac{dy(t, x)}{dt} = f(t, x, y(t, x)), \quad y(t_0, x) = y_0(x). \quad (4.1)$$

The photon PDFs however are inhomogeneous DE due to the point-like contribution, i.e.

$$\frac{dy(t, x)}{dt} = f(t, x, y(t, x)) + f_{\text{PL}}(t, x) = f'(t, x, y(t, x)), \quad y(t_0, x) = y_0(x). \quad (4.2)$$

The calculation of these DEs is done by using the *Runge-Kutta 4 method*, inside the function `EvolveObject` in `matchedevolution.cc`. Originally in APFEL++ the *RK4 method* only has a function as input, which returns `Derivative` of the PDFs at a given  $t$ . The function `Derivative` returns  $f(t, x, y(t, x))$ .

By simply adding  $f_{\text{PL}}(t, x)$  to `Derivative`, i.e. adding the point-like term to the right-handside of the hadronic DGLAP evolution equation, `EvolveObject` now calculates inhomogeneous DEs, i.e. the photon PDFs.

The point-like contributions, which are added to the hadronic part, can be seen in eqs. (3.5) and (3.9). However, since APFEL++ uses the QCD evolution basis, and these point-like contributions are in the physical basis, the conversion still has to be calculated.

#### 4.1.1. QCD Evolution Basis

In the following part the  $x$ -dependence of the PDFs will not be explicitly mentioned. APFEL++ does all calculations in a basis called QCD evolution basis. This basis is given in eqs. (4.3) to (4.5):

$$g = g \quad (4.3)$$

$$\begin{aligned}
\Sigma &= \sum_q q^+ \\
T_3 &= u^+ - d^+ \\
T_8 &= u^+ + d^+ - 2s^+ \\
T_{15} &= u^+ + d^+ + s^+ - 3c^+ \\
T_{24} &= u^+ + d^+ + s^+ + c^+ - 4b^+ \\
T_{35} &= u^+ + d^+ + s^+ + c^+ + b^+ - 5t^+
\end{aligned} \tag{4.4}$$

$$\begin{aligned}
V &= \sum_q q^- \\
V_3 &= u^- - d^- \\
V_8 &= u^- + d^- - 2s^- \\
V_{15} &= u^- + d^- + s^- - 3c^- \\
V_{24} &= u^- + d^- + s^- + c^- - 4b^- \\
V_{35} &= u^- + d^- + s^- + c^- + b^- - 5t^-
\end{aligned} \tag{4.5}$$

with  $q^\pm = q \pm \bar{q}$ .

To get the DGLAP equations in this basis, the first step is to calculate how the  $q^\pm$  relate to  $q_{NS}$  and  $\Sigma$ .

We know that

$$q_{NS}^{(n_f)} = \sum_{q=1}^{n_f} (e_q^2 - \langle e^2 \rangle) (q + \bar{q}), \tag{4.6}$$

where the  $n_f$  at the  $q_{NS}$  is introduced for later book keeping. Now, using a function

$$c_q^{(n_f)} := e_q^2 - \langle e^2 \rangle = e_q^2 - \frac{1}{n_f} \sum_{q=1}^{n_f} e_q^2, \tag{4.7}$$

we can rewrite the  $q_{NS}^{(n_f)}$ , for example:

$$q_{NS}^{(2)} = c_u^{(2)} u^+ + c_d^{(2)} d^+. \tag{4.8}$$

From this it is now possible to calculate equations for  $u^+, s^+, c^+, b^+, t^+$ , only dependent on  $d^+$  and  $q_{NS}$  at different  $n_f$ . It would be possible as well to calculate  $d^+$  but this is not necessary for the following calculations.

Starting from  $q_{NS}^{(2)}$  and then going to higher  $n_f$  we can calculate the aforementioned equations. The calculation of  $u^+$  is given as an example:

$$\begin{aligned} u^+ &= \frac{q_{NS}^{(2)}}{c_u^{(2)}} - \frac{c_d^{(2)}}{c_u^{(2)}} d^+ \\ &= \frac{q_{NS}^{(2)}}{c_u^{(2)}} + d^+ \end{aligned} \quad (4.9)$$

The resulting equations are:

$$\begin{aligned} u^+ &= \frac{q_{NS}^{(2)}}{c_u^{(2)}} + d^+ \\ s^+ &= \frac{2q_{NS}^{(2)}}{c_u^{(2)}} + \frac{q_{NS}^{(3)}}{c_s^{(3)}} + d^+ \\ c^+ &= \frac{q_{NS}^{(2)}}{c_u^{(2)}} + \frac{q_{NS}^{(3)}}{c_s^{(3)}} + \frac{q_{NS}^{(4)}}{c_c^{(4)}} + d^+ \\ b^+ &= \frac{q_{NS}^{(2)}}{c_u^{(2)}} + \frac{q_{NS}^{(3)}}{2c_s^{(3)}} + \frac{3q_{NS}^{(4)}}{2c_c^{(4)}} + \frac{q_{NS}^{(5)}}{c_b^{(5)}} + d^+ \\ t^+ &= \frac{q_{NS}^{(2)}}{c_u^{(2)}} + \frac{q_{NS}^{(3)}}{2c_s^{(3)}} + \frac{q_{NS}^{(4)}}{2c_c^{(4)}} + \frac{q_{NS}^{(5)}}{c_b^{(5)}} + \frac{q_{NS}^{(6)}}{c_t^{(6)}} + d^+ \end{aligned} \quad (4.10)$$

From these equations the QCD evolution basis can now be calculated.

$\Sigma$  : already given

$$\begin{aligned} T_3 &= \frac{q_{NS}^{(2)}}{c_u^{(2)}} && \text{for } n_f \leq 2 \\ T_8 &= -\frac{2q_{NS}^{(3)}}{c_s^{(3)}} - \frac{3q_{NS}^{(2)}}{c_u^{(2)}} && \text{for } n_f \leq 3 \\ T_{15} &= -\frac{3q_{NS}^{(4)}}{c_c^{(4)}} - \frac{2q_{NS}^{(3)}}{c_s^{(3)}} && \text{for } n_f \leq 4 \\ T_{24} &= -\frac{4q_{NS}^{(5)}}{c_b^{(5)}} - \frac{5q_{NS}^{(4)}}{c_c^{(4)}} && \text{for } n_f \leq 5 \\ T_{35} &= -\frac{5q_{NS}^{(6)}}{c_t^{(6)}} - \frac{4q_{NS}^{(5)}}{c_b^{(5)}} && \text{for } n_f \leq 6 \end{aligned} \quad (4.11)$$

The equations which require higher  $n_f$  than the current (i.e.  $Q^2$  has not surpassed the threshold of all included quarks) simplify to  $\Sigma$ , i.e.

$$T_{15}^{(n_f=3)} = u^+ + d^+ + s^+ - 3c^+ = u^+ + d^+ + s^+ = \Sigma^{(n_f=2)}. \quad (4.12)$$

All valence-terms (see eq. (4.5)) are zero, since the quark and anti-quark are set to have the same PDFs in the real photon, i.e.

$$q^- = q - \bar{q} = 0. \quad (4.13)$$

#### 4.1.2. Continuation of Implementation

Using the procedure shown in section 4.1.1 the DGLAP equations in the QCD evolution basis can be calculated, e.g.:

$$\begin{aligned} \frac{dT_{15}}{d \ln Q^2} &= -\frac{3}{c_c^{(4)}} \frac{dq_{NS}^{(4)}}{d \ln Q^2} - \frac{2}{c_s^{(3)}} \frac{dq_{NS}^{(3)}}{d \ln Q^2} \\ &= -\frac{\alpha_s}{2\pi} P_{NS} \otimes \left( \frac{3}{c_c^{(4)}} q_{NS}^{(4)} + \frac{2}{c_s^{(3)}} q_{NS}^{(3)} \right) - \frac{\alpha}{2\pi} \left( \frac{3}{c_c^{(4)}} k_{NS}^{(4)} + \frac{2}{c_s^{(3)}} k_{NS}^{(3)} \right) \\ &= -\frac{\alpha_s}{2\pi} P_{NS} \otimes T_{15} - \frac{\alpha}{2\pi} \left( \frac{3}{c_c^{(4)}} k_{NS}^{(4)} + \frac{2}{c_s^{(3)}} k_{NS}^{(3)} \right), \end{aligned} \quad (4.14)$$

where

$$\begin{aligned} k_{NS}^{(n_f)} &= k_{NS}^{(0,n_f)} + \frac{\alpha_s}{2\pi} k_{NS}^{(1,n_f)} \\ P_{NS} &= P_{qq}^{(0)} + \frac{\alpha_s}{2\pi} P_{qq}^{(1)}. \end{aligned} \quad (4.15)$$

This means that it is now known, in which way the point-like contributions in the QCD evolution basis can be calculated from the ones in the physical basis.

At this point it is worth mentioning that the PDFs in **APFEL++** are used as  $\text{PDF} \cdot \frac{x}{\alpha}$ , which has to be accounted for aswell, but is not shown here.

With these changes done to **APFEL++**, it can now evolve photon PDFs. Using a file like `Evolution.cc` provided in [14] or the `EvolutionLHAPDF.cc` file in the GitHub repository [15], **APFEL++** can now evolve photon PDFs from LHAPDF files. By using a file like `Evolution.cc` in the GitHub repository it is also possible to evolve initial PDFs (PDFs given at the input scale  $Q_0$ ) with given parameters.

## 4.2. Input

To compare **APFEL++**'s results for the evolution of the PDFs to the results of GRV, the following parameters were used:

$$\begin{aligned} Q_0 &= 1.3 \text{ GeV} & m_b &= 4.5 \text{ GeV} \\ m_c &= 1.5 \text{ GeV} & m_t &= 100 \text{ GeV}. \end{aligned} \quad (4.16)$$

The masses of the quarks are the same that GRV [16] used. The  $Q_0$  is the same as used by nCTEQ15 [17] and will always be used from now on.

GRV used a fixed equation for  $\alpha_s$  [7]

$$\frac{4\pi}{\alpha_s(Q^2)} = \beta_0 \ln \frac{Q^2}{\Lambda^2} + \frac{\beta_1}{\beta_0} \ln \ln \frac{Q^2}{\Lambda^2}, \quad (4.17)$$

instead of evolving it from an input scale like *APFEL++* does. Therefore, to compare the GRV and *APFEL++* results, it is wise to use the same method for the calculation of  $\alpha_s$  as GRV. This was only done for the results shown in section 4.3.

The PDF values calculated by GRV were saved as a LHAPDF set using the parameters given in [16]. Then they were evolved from the input scale up to the desired energy where they can be compared to the LHAPDF values of GRV at the same energy.

### 4.3. Results

Using the inputs given in section 4.2 the results in figs. 8 and 9 were calculated. These plots show that the modified *APFEL++* code does reproduce the results from GRV very well. This shows that the evolution of the PDFs itself does work.

There was also a cross check done with a modified version of QCDNUM by Vadim Guzey (for the QCDNUM results see [3]) which yielded very good results. This cross check however will not be shown here.

Therefore the functionality of the evolution of photon PDFs is validated.

#### 4. Numerical Implementation of the Evolution of Photon PDFs using *APFEL++*

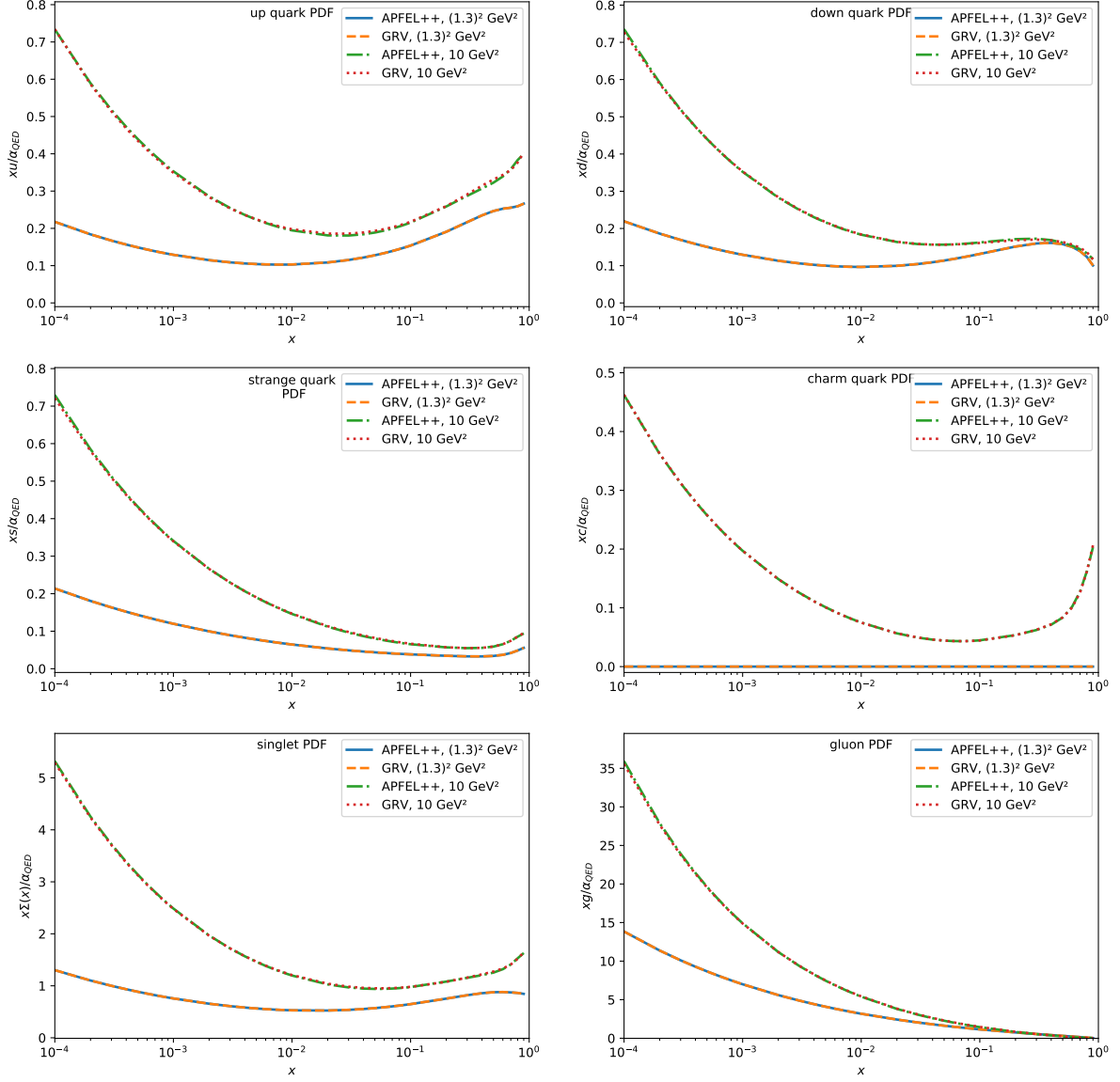


**Figure 8:** PDFs calculated using the inputs from section 4.2 at  $Q^2 = (1.3 \text{ GeV})^2$  and  $Q^2 = 10 \text{ GeV}^2$  for LO. The lines for APFEL++ are partially hidden behind the ones for GRV.



#### 4. Numerical Implementation of the Evolution of Photon PDFs using *APFEL++*

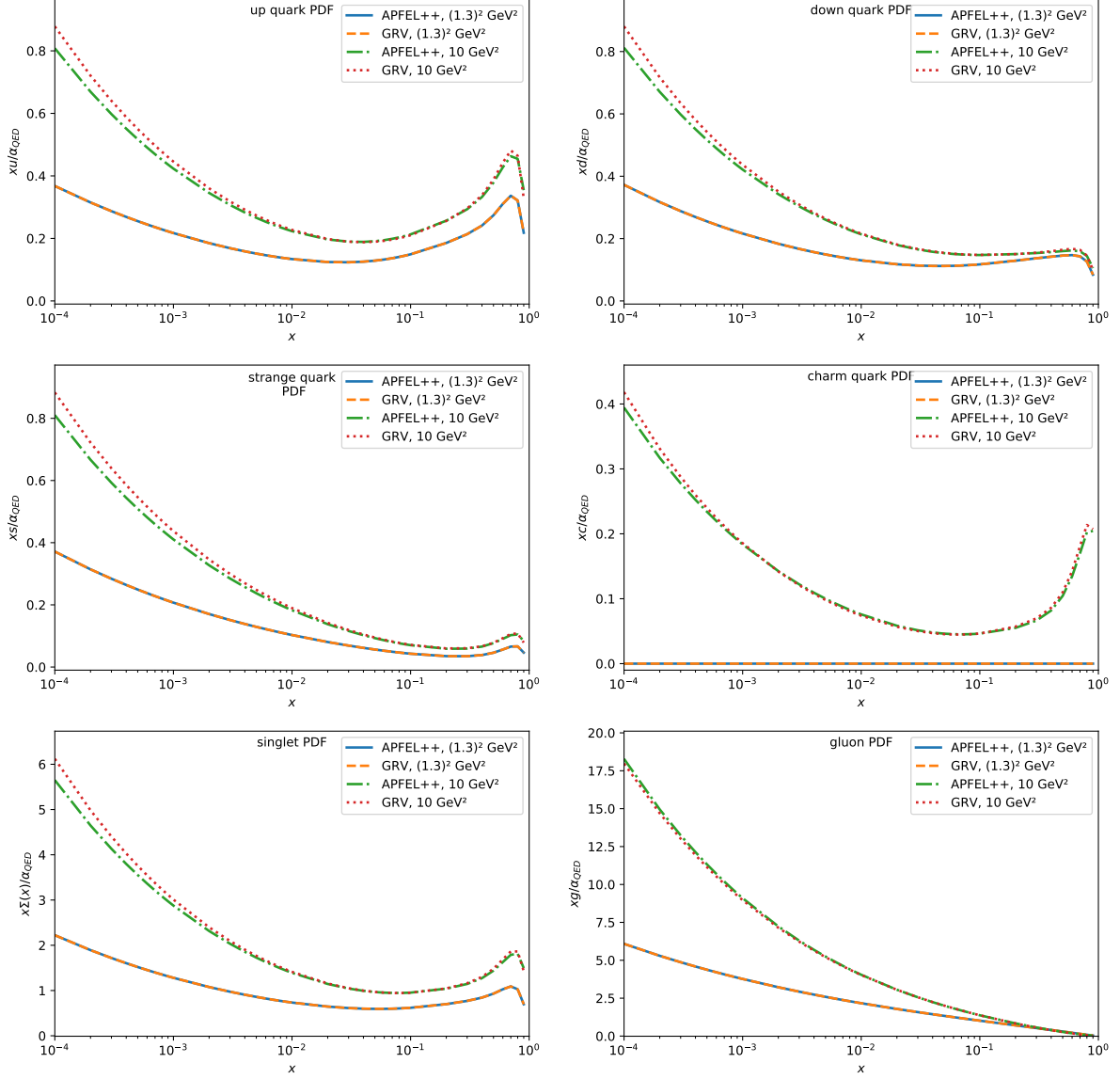


**Figure 9:** PDFs calculated using the inputs from section 4.2 at  $Q^2 = (1.3 \text{ GeV})^2$  and  $Q^2 = 10 \text{ GeV}^2$  for HO. The lines for *APFEL++* are partially hidden behind the ones for GRV.

## 5. Fitting of Initial Parameters using $\chi^2$ -Minimization

Now that the photon PDFs can be evolved, the next step is to write a program which takes input PDFs with free parameters and calculates the structure functions from them. The program can be used to fit the free parameters of the input PDFs to the experimental data. This fit is done using a MINUIT C++ library [18].

### 5.1. Input PDFs

The input PDFs are motivated by SAL [12]. They are given by

$$\begin{aligned}
 \frac{1}{\alpha} x \bar{u}^\gamma(x, Q_0) &= A_q^{\text{had}} x^{B_q^{\text{had}}} (1-x)^{C_q^{\text{had}}} + A_q^{\text{PL}} e_u^2 x \frac{x^2 + (1-x)^2}{1 - B_q^{\text{PL}} \ln(1-x)} \\
 \frac{1}{\alpha} x \bar{d}^\gamma(x, Q_0) &= A_q^{\text{had}} x^{B_q^{\text{had}}} (1-x)^{C_q^{\text{had}}} + A_q^{\text{PL}} e_d^2 x \frac{x^2 + (1-x)^2}{1 - B_q^{\text{PL}} \ln(1-x)} \\
 \frac{1}{\alpha} x \bar{s}^\gamma(x, Q_0) &= K_s A_q^{\text{had}} x^{B_q^{\text{had}}} (1-x)^{C_q^{\text{had}}} + A_q^{\text{PL}} e_s^2 x \frac{x^2 + (1-x)^2}{1 - B_q^{\text{PL}} \ln(1-x)} \\
 \frac{1}{\alpha} x g^\gamma(x, Q_0) &= A_g^{\text{had}} x^{B_g^{\text{had}}} (1-x)^{C_g^{\text{had}}}.
 \end{aligned} \tag{5.1}$$

Since too many free parameters could lead to overfitting, some of them will be fixed. The parameters  $C_q^{\text{had}}$  and  $C_g^{\text{had}}$  are set to  $C_q^{\text{had}} = 1$  and  $C_g^{\text{had}} = 3$  as done by SAL [12]. These values are suggested by counting rules based on dimensional arguments. Another parameter adopted by SAL is  $K_s = 0.3$ .

With these assumptions there are 6 free parameters left; the same number as SAL has. The fixed parameters are the same as used by SAL as well.

However, as will be discussed in more detail in section 5.2, the parameter  $A_g^{\text{had}}$  will be determined by the momentum sum rule and is therefore not free. This leaves at most 5 free parameters:  $A_q^{\text{had}}, B_q^{\text{had}}, A_q^{\text{PL}}, B_q^{\text{PL}}$  and  $B_g^{\text{had}}$ .

For the calculations three different input PDFs are used: Fit3, Fit4 and Fit5. The number refers to the number of free parameters.

Fit5 includes all free parameters. Fit3 sets the free parameters belonging to the point-like part of the PDFs to zero, i.e.  $A_q^{\text{PL}} = B_q^{\text{PL}} = 0$ . Fit4 only sets  $B_q^{\text{PL}}$  to zero.

The three input PDFs can be seen in appendix A.2.

In the code Fit3, Fit4 and Fit5 are referred to as SAL3, SAL4 and SAL5.

## 5.2. Momentum Sum Rule

To ensure the momentum sum rule, the parameter  $A_g^{\text{had}}$  (see section 5.1) will not be chosen by MINUIT. Rather it is calculated from the other parameters using the FG momentum sum rule [12]

$$\frac{1}{\alpha_{\text{em}}} \int_0^1 dx x [\Sigma(x, Q^2) + G(x, Q^2)] \approx 1 + \frac{2}{3\pi} \ln \frac{Q^2}{4 \text{ GeV}^2}, \quad (5.2)$$

where  $\Sigma$  is the singlet PDF and  $G$  the one for the gluon.

From this the  $A_g^{\text{had}}$  can be calculated:

$$\begin{aligned} A_g^{\text{had}} &= [\text{r.h.s.} - 2(2 + K_s) \text{l.h.s.}_q^{\text{had}} - 2(e_u^2 + e_d^2 + e_s^2) \text{l.h.s.}_q^{\text{PL}}] / \text{l.h.s.}_g^{\text{had}} \\ \text{r.h.s.} &= 1 + \frac{2}{3\pi} \ln \frac{Q^2}{4 \text{ GeV}^2} \\ \text{l.h.s.}_g^{\text{had}} &= \int_0^1 x^{B_g^{\text{had}}} (1-x)^{C_g^{\text{had}}} = \mathcal{B}(B_g^{\text{had}} + 1, C_g^{\text{had}} + 1) \\ \text{l.h.s.}_q^{\text{had}} &= A_q^{\text{had}} \int_0^1 x^{B_q^{\text{had}}} (1-x)^{C_q^{\text{had}}} = A_q^{\text{had}} \mathcal{B}(B_q^{\text{had}} + 1, C_q^{\text{had}} + 1) \\ \text{l.h.s.}_q^{\text{PL}} &= A_q^{\text{PL}} x \frac{x^2 + (1-x)^2}{1 - B_q^{\text{PL}} \log(1-x)} \\ &= \begin{cases} \frac{A_q^{\text{PL}}}{3} & \text{for } B_q^{\text{PL}} = 0 \\ -\frac{A_q^{\text{PL}}}{B_q^{\text{PL}}} (F_1 - 3F_2 + 4F_3 - 2F_4) & \text{for } B_q^{\text{PL}} \neq 0 \end{cases} \end{aligned} \quad (5.3)$$

with the Beta function

$$\mathcal{B}(z_1, z_2) = \frac{\Gamma(z_1) \Gamma(z_2)}{\Gamma(z_1 + z_2)} \quad (5.4)$$

and

$$F_n = \exp(n/B_q^{\text{PL}}) \text{Ei}(-n/B_q^{\text{PL}}), \quad (5.5)$$

where Ei is the Exponential Integral.

## 5.3. Implementation

As mentioned in section 3.4, the structure function  $F_2^\gamma$  in the  $\text{DIS}_\gamma$  factorization scheme is the same as in the hadronic/proton case [16]. Therefore the structure functions do not have to be changed in APFEL++ and one can simply use the function `InitializeF2NCObjectsZM` when initializing the structure functions.

There is however an equation for  $F_2^\gamma$  which eliminates spurious higher order terms [16], but the difference is said to be not significant. This will not be used.

As already mentioned the fitting of the free parameters is done using MINUIT (C++ library *minuit-cpp* [18]). MINUIT fits these parameters by minimizing the  $\chi^2$  function.

The program starts with input PDFs, which have to be given by the user. They can have an arbitrary but fixed number of free parameters. The input PDFs used in this thesis are given in section 5.4. For these free parameters the user can set a range in which the final value will lie in as well as a starting value. The range of these parameters are motivated mostly by physical considerations (i.e. PDFs have to be positive). They are discussed in section 5.4.1.

With these starting values the input PDFs are evolved in  $Q^2$  and the  $F_2^\gamma$  structure functions are calculated. The calculated  $F_2^{\gamma,calc.}$  values and the experimental  $F_2^{\gamma,exp.}$  values are then used to calculate the  $\chi^2$  function:

$$\chi^2(\alpha) = \sum_{i=1}^n \frac{\left(F_2^{\gamma,calc.}(x_i, Q_i, \alpha) - F_{2,i}^{\gamma,exp.}\right)^2}{\sigma_i^2}, \quad (5.6)$$

where  $\sigma_i$  is the uncertainty on the measured value  $F_{2,i}^{\gamma,exp.}$ .

By varying the values of the free parameters within the given range, MINUIT determines the optimal set of parameters  $\{a_i^0\}$  for which the  $\chi^2$  is minimal, i.e.

$$\chi^2(\{a_i^0\}) = \chi_0^2. \quad (5.7)$$

## 5.4. Input

### 5.4.1. Initial Free Parameters

The free parameters of the input PDFs all have the initial value 0.5. Their initial error is 0.1.

The boundaries for the free parameters are:

$$\begin{aligned} 0 &\leq A_q^{\text{had}} \leq 40 & 0 &\leq A_q^{\text{PL}} \leq 40 \\ -1 &\leq B_q^{\text{had}} \leq 1 & 0 &\leq B_q^{\text{PL}} \leq 40 \\ -1 &\leq B_g^{\text{had}} \leq 1 & & \end{aligned} \quad (5.8)$$

The upper boundaries of 40 were chosen big enough to have no effect on the result but small enough that the minimization does not take too long.

### 5.4.2. Evolution Parameters

The used parameters for the evolution are:

$$\begin{aligned}
 Q_0 &= 1.3 \text{ GeV} & m_b &= 4.5 \text{ GeV} \\
 m_c &= 1.3 \text{ GeV} & m_t &= 174 \text{ GeV} \\
 Q_{\text{ref}} &= m_Z = 91.188 \text{ GeV} & \alpha_{s,\text{ref}} &= \alpha_s(Q_{\text{ref}}) = 0.1179973.
 \end{aligned}
 \tag{5.9}$$

These parameters are the same as used by nCTEQ15 [17].

### 5.4.3. Used Data on $F_2^\gamma$

**Table 1:** Available experimental Data on  $F_2^\gamma$  structure function. The  $Q^2$  values written in *italics* are values left out. Please note that the values for OPAL2 (without the left out values) are called OPAL2\_less in the code as an artifact of earlier versions.

	Facility	Experiment	$\langle Q^2 \rangle$ , GeV <sup>2</sup>	# points	Used # points	Name
1	LEP (CERN)	ALEPH [19]	9.9, 20.7, 284	11	11	ALEPH1
2		ALEPH [20]	17.3, 67.2	16	16	ALEPH2
3		DELPHI [21]	12	4	4	DELPHI
4		L3 [22]	1.9, 5	12	12	L3
5		L3 [23]	10.8, 15.3, 23.1	11	11	
6		OPAL [24]	7.5, 14.7, 135	10	10	OPAL1
7		OPAL [25]	9, 14.5, 30, 59	14	14	
8		OPAL [26]	1.86, 3.76	8	8	
9		OPAL [27]	5.9, 14.7	7	7	OPAL2
10		OPAL [28]	<i>1.9, 3.7, 8.9, 10.7, 17.5, 17.8</i>	22	0	
11		OPAL [29]	<i>12.1, 19.9, 39.7, 76.4, 780</i>	13	3	
12	TRISTAN (Japan)	AMY [30, 31]	73, 390	5	5	AMY
13		AMY [32]	6.8	3	3	
14		TOPAZ [33]	5.1, 16, 80	8	8	TOPAZ
15	PETRA (DESY)	JADE [34]	24, 100	8	8	JADE
16		PLUTO [35]	2.4, 4.3, 9.2, 5.3	15	15	PLUTO
17		PLUTO [36]	45	4	4	
18		TASSO [37]	23	5	5	TASSO
19	PEP (SLAC)	TPC/2 $\gamma$ [38]	<i>0.24, 0.38, 0.71, 1.3, 2.8, 5.1</i>	22	0	TPC
	Total # points			198	144	

All the data available on the  $F_2^\gamma(x, Q^2)$  structure function can be seen in table 1. However not all of the data was used for the fitting as indicated in the table.

Since the input scale of  $Q_0^2 = (1.3)^2 \text{ GeV}^2 = 1.69 \text{ GeV}^2$  is bigger than some of the  $Q^2$  values of the TPC/2 $\gamma$  data [38], these data points can not be used. Furthermore, as can be seen by running the minimization of the  $\chi^2$  and looking at the contributions of each experiment, the TPC/2 $\gamma$  data is inconsistent with the rest. This inconsistency with other measurements (in particular PLUTO, L3 and OPAL) is discussed in previous literature as well [39, 40]. Hence, all data from TPC/2 $\gamma$  is excluded from further calculations.

## 5. Fitting of Initial Parameters using $\chi^2$ -Minimization

---

**Table 2:** Parameters calculated for the input PDFs for the inputs given in section 5.4.

	Fit3		Fit4		Fit5	
	LO	HO	LO	HO	LO	HO
$A_g^{\text{had}}$	0.162077	0.162793	0.427143	0.267262	0.482187	0.243060
$B_g^{\text{had}}$	-0.384581	-0.182473	-0.224452	-0.215028	-0.202210	-0.272855
$C_g^{\text{had}}$	3	3	3	3	3	3
$A_q^{\text{had}}$	0.439775	0.471788	0.436453	0.491192	0.524953	0.591875
$B_q^{\text{had}}$	0.256241	0.263275	0.570871	0.505920	0.665115	0.610880
$C_q^{\text{had}}$	1	1	1	1	1	1
$A_q^{\text{PL}}$	0	0	0.320468	0.247174	0.348421	0.297112
$B_q^{\text{PL}}$	0	0	0	0	0.648468	1.116165
$K_s$	0.3	0.3	0.3	0.3	0.3	0.3

Using the  $\chi^2$  analysis some other data could be identified to lead to large  $\chi^2$  values. This is in particular the small- $x$  data from OPAL [28]. Furthermore the most recent data from the OPAL collaboration [29] seems to be not fully compatible with their earlier data [25]. Therefore the latest OPAL data [29] is not used. An exception to this are the three data points at  $Q^2 = 780 \text{ GeV}^2$  since they uniquely constrain the  $F_2^\gamma(x, Q^2)$  structure functions at very large values of  $Q^2$ .

To sum it up the small- $x$  data and the most recent data (except for  $Q^2 = 780 \text{ GeV}^2$ ) from the OPAL collaboration are excluded from further calculations.

This leads to a total of 144 used data points out of 198 possible.

### 5.5. Results

Using the inputs given in section 5.4 the following initial PDFs (i.e. input PDFs with initial parameters) are calculated (see figs. 10 and 11).

The calculated initial parameters, the parameters for which the overall  $\chi^2$  was the minimum, can be seen in table 2. The corresponding  $\chi^2$  values (including the  $\chi^2$  values for each experiment) are shown in table 4 and the  $\chi^2$  values per degree of freedom in table 3.

## 5. Fitting of Initial Parameters using $\chi^2$ -Minimization

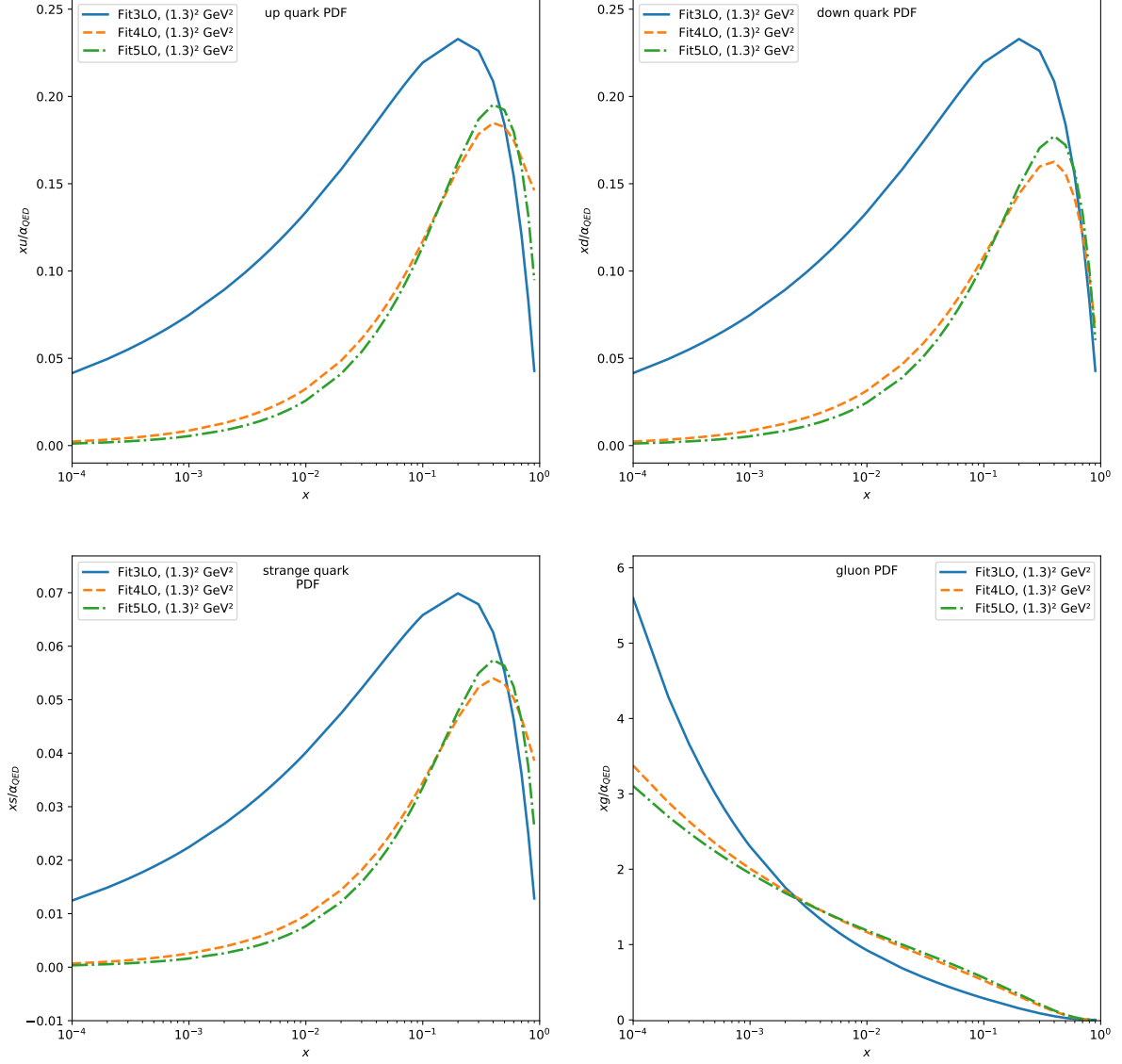


**Figure 10:** Initial PDFs calculated using the inputs and data from section 5.4 for LO.

## 5. Fitting of Initial Parameters using $\chi^2$ -Minimization

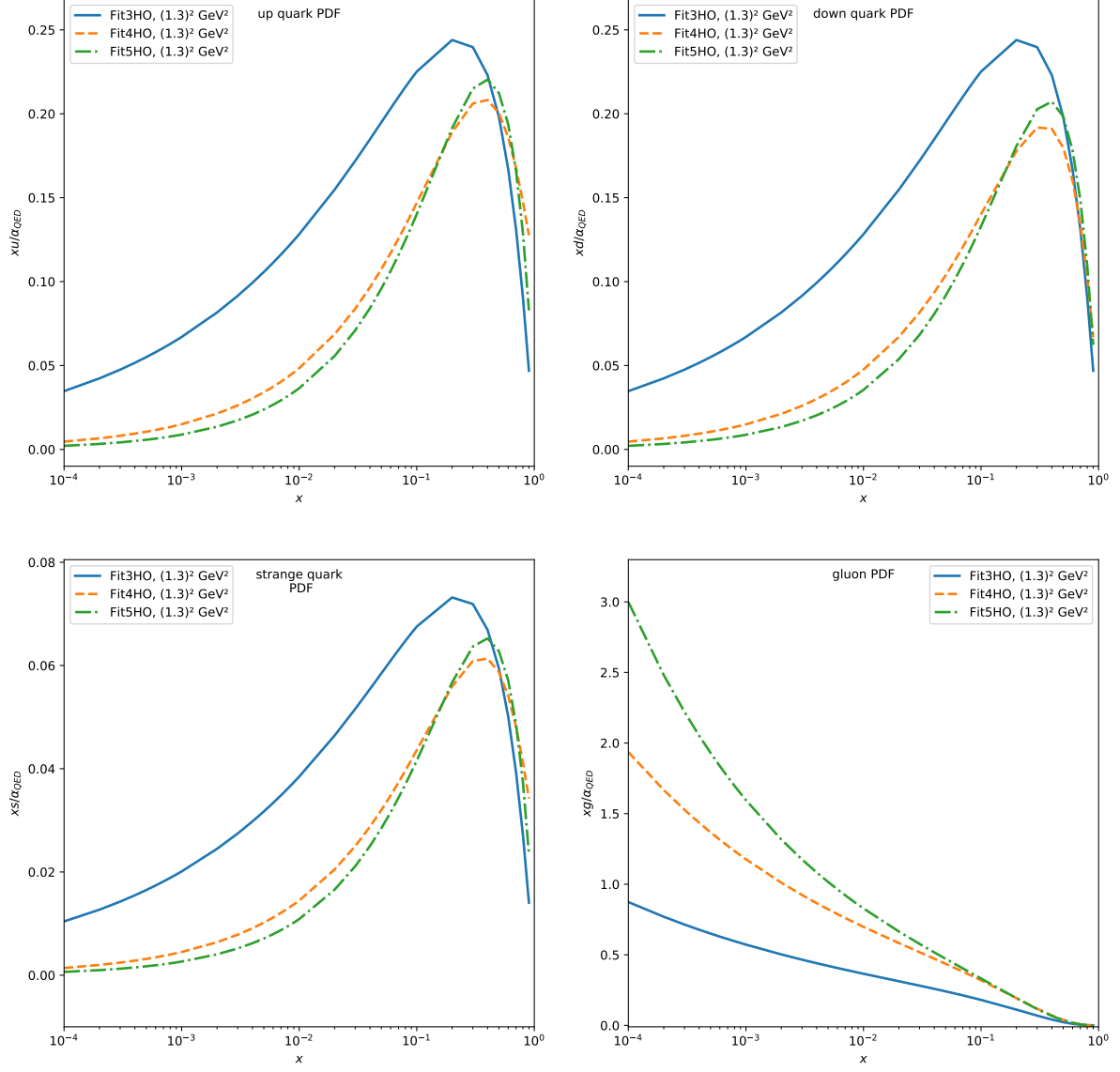


**Figure 11:** Initial PDFs calculated using the inputs and data from section 5.4 for HO.



**Table 3:** Global  $\chi^2$  per degree of freedom and  $\chi^2$  per degree of freedom for each experiment for the calculated initial parameters given in table 2. The global  $\chi^2$  is included aswell.

	Fit3		Fit4		Fit5	
	LO	HO	LO	HO	LO	HO
$\chi^2$	129.127	122.271	113.702	116.328	109.416	111.309
$\chi^2$ per d.o.f.	0.896717	0.849104	0.7896	0.807835	0.759835	0.772977
ALEPH1	0.421091	0.426659	0.476703	0.495389	0.450164	0.479691
ALEPH2	0.963674	0.893105	0.811291	0.853296	0.748735	0.789305
AMY	0.744302	1.002104	0.903917	1.209668	0.844452	1.144132
DELPHI	0.672708	0.884293	0.662400	0.883335	0.652354	0.871593
JADE	1.583556	2.029574	1.875657	2.325547	1.743700	2.217579
L3	1.355817	0.900927	0.968091	0.599797	0.941752	0.574012
OPAL1	0.412068	0.380778	0.322756	0.322407	0.311830	0.305648
OPAL2	0.860177	1.138335	0.854554	1.143037	0.803848	1.095700
PLUTO	0.641030	0.397736	0.371374	0.306365	0.408288	0.306797
TASSO	1.470840	1.571826	1.336956	1.568040	1.276440	1.461923
TOPAZ	1.907161	1.973974	1.963891	2.025911	1.919130	1.993053

## 6. Calculation of Error PDFs

### 6.1. Implementation

Now that the optimal set of parameters for the input PDFs is obtained, it is helpful to look at the uncertainties of these PDFs. The method used for calculating the so called error PDFs is called the Hessian method.

The description of this method follows nCTEQ15 [17].

The goal of the Hessian method is to calculate the  $2n$  error PDFs, where  $n$  is the number of free parameters  $a_i$ . These error PDFs most importantly depend on the tolerance  $\Delta\chi^2$  and the eigenvectors and -values of the Hessian matrix of the  $\chi^2$ .

#### 6.1.1. Hessian Matrix

The Hessian matrix of the  $\chi^2$  is given by

$$H_{i,j} = \frac{1}{2} \left( \frac{\partial^2 \chi^2}{\partial y_i \partial y_j} \right)_{a_i=a_i^0}, \quad (6.1)$$

where  $y_i = a_i - a_i^0$  are the free parameters  $a_i$  but centered around  $a_i^0$ .  $a_i^0$  are the  $n$  free parameters, which result in the lowest overall  $\chi^2$ , i.e.  $\chi^2(\{a_i^0\}) = \chi_0^2$  (see table 2).

The calculation is done by calculating the second derivative of the  $\chi^2$  function using the standard central differences method (step width  $h = 0.005$ ). The results of these derivatives are saved in a matrix using the *Eigen*-library. In the next step the  $n$  eigenvectors  $V^{(k)}$  and eigenvalues  $\lambda_k$  are calculated using this library aswell.

### 6.1.2. Tolerance $\Delta\chi^2$

The tolerance  $\Delta\chi^2$  is the difference of the  $\chi^2$  with some specific free parameters and the ideal free parameters, i.e.  $\Delta\chi^2 = \chi^2 - \chi_0^2$ . As explained in for example [41], for a truly global PDF analysis the choice of  $\Delta\chi^2 = 1$ , as done in the statistically ideal case, is not sufficient, since this analysis tries to include as many independent experiments as possible. Therefore it is necessary to calculate the tolerance for each set of initial PDFs.

The first goal for obtaining  $\Delta\chi^2$  is to calculate  $\xi_p$ .  $\xi_p$  is the value where there is a probability of  $p\%$  for a set of parameters, which results in  $\chi^2 < \xi_p$ , to genuinely describe the given data. It can be calculated by solving

$$\int_0^{\xi_p} P(\chi_k^2, N_k) d\chi_k^2 = p\%, \quad (6.2)$$

where  $\chi_k^2$  is the contribution of the experiment  $k$  with  $N_k$  datapoints to  $\chi^2$ . The probability distribution for  $\chi_k^2$  is

$$P(\chi_k^2, N_k) = \frac{(\chi_k^2/2)^{N_k/2-1} e^{-\chi_k^2/2}}{2 \cdot \Gamma(N_k/2)}. \quad (6.3)$$

The solution of eq. (6.2) is the normalized lower incomplete gamma function

$$\frac{\gamma(a, x)}{\Gamma(a)} = \frac{\int_0^x t^{a-1} e^{-t} dt}{\Gamma(a)}, \quad (6.4)$$

using  $a = N_k/2$ ,  $x = \xi_p$  and  $t = \chi_k^2/2$ . Therefore, to calculate  $\xi_p$ , one has to calculate the inverse of the normalized lower incomplete gamma function.

These calculations are done using the *boost*-library in C++. The function `gamma_p(a, x)` is the normalized lower incomplete gamma function of  $a$  and  $x$  and `gamma_p_inv(a, p)` is the inverse of it. This means that

$$\text{gamma\_p\_inv}(N_k/2, p\%) = \xi_p. \quad (6.5)$$

For the same reasons as given in [17, Appendix A] the  $\xi_p$  have to be rescaled here as well. The  $\xi_{90}$ , which will be used later, therefore becomes

$$\tilde{\xi}_{90} \rightarrow \xi_{90} \left( \frac{\chi_{k,0}^2}{\xi_{50}} \right), \quad (6.6)$$

where  $\chi_{k,0}^2$  is the contribution of experiment  $k$  to the global minimum  $\chi_0^2$ , i.e.  $\chi_{k,0}^2 = \chi_k^2(\{a_i^0\})$  (see table 4).

At this point it is sensible to introduce a new basis  $\mathbf{z} \equiv \{z_i\}$ . This basis is defined such that the Hessian becomes diagonal. The relation to  $\{y_i\}$  is

$$y_i = \sum_j V_i^{(j)} z_j \equiv \sum_j V_i^{(j)} \frac{\tilde{z}_j}{\sqrt{\lambda_j}}, \quad (6.7)$$

where  $\tilde{z}_i = \sqrt{\lambda_i} z_i$  is a new, rescaled basis. The inverse transformations are given by

$$z_i = \sum_j y_j V_j^{(i)} \quad (6.8)$$

$$\tilde{z}_i = \sqrt{\lambda_i} \sum_j y_j V_j^{(i)}. \quad (6.9)$$

This means that just as for  $\{y_i\}$ ,  $\{z_i\}$  and  $\{\tilde{z}_i\}$  become zero for  $a_i = a_i^0$ .

For the next step in determining  $\Delta\chi^2$  one has to calculate an interval

$$z_i^{(k)-} \leq \tilde{z}_i \leq z_i^{(k)+} \quad (6.10)$$

for each eigenvector direction and experiment, where  $\chi_k^2$  stays smaller than  $\tilde{\xi}_{90}$ . This means that the probability for each  $\tilde{z}_i$  in this interval to genuinely describe the data of experiment  $k$  is at least 90%.

With these intervals the interval  $(z_i^-, z_i^+)$  can now be calculated for each eigenvector direction. This interval spans over all  $\tilde{z}_i$  where  $\chi_k^2 < \tilde{\xi}_{90}$  for all experiments  $k$ , meaning that the probability for each  $\tilde{z}_i$  in this interval to genuinely describe the data of **all** considered experiments is at least 90%:

$$(z_i^-, z_i^+) \equiv \bigcap_k (z_i^{(k)-}, z_i^{(k)+}). \quad (6.11)$$

Finding these intervals is computationally quite an intensive part of the program. The calculation time of this function however is lessened by immediately calculating the interval in eq. (6.11) and skipping the calculation of eq. (6.10).

It is implemented as follows:

- the function receives as inputs, amongst others, the optimal free parameters  $\{a_j^0\}$ , the index  $i$  of the parameter  $\tilde{z}_i$ , a stepsize and a precision
- the default for the stepsize is 100 and for the precision  $10^{-6}$
- in the beginning of the function the variation of the parameter  $\tilde{z}_i$ ,  $\Delta z$ , is set to zero

- after that the function moves through the following steps:
  1. if the stepsize is larger or equal to the precision, increase  $\Delta z$  by the stepsize, otherwise the function ends
  2. calculate  $\{\tilde{z}_j\}$  for  $a_j = a_j^0$  (i.e. set all  $\tilde{z}_j$  to zero) and add/subtract  $\Delta z$  to/from  $\tilde{z}_i$ , depending on if  $z_i^+$  or  $z_i^-$  is being calculated
  3. transform  $\{\tilde{z}_j\}$  to  $\{a_j\}$  and calculate the  $\chi_k^2$  from these values
  4. compare each  $\chi_k^2$  to its corresponding  $\tilde{\xi}_{90}$
  5. if  $\chi_k^2 \geq \tilde{\xi}_{90}$  holds for no experiment, increase  $\Delta z$  by the stepsize and go to step 2
  6. if however there is at least one experiment for which  $\chi_k^2 \geq \tilde{\xi}_{90}$  holds, meaning the probability that the parameters  $\{\tilde{z}_j\}$  with  $\Delta z$  added to  $\tilde{z}_i$  genuinely describe the data of an experiment is lower than 90%, then subtract the stepsize from  $\Delta z$  (because the  $\Delta z$  for which  $\chi_k^2 < \tilde{\xi}_{90}$  holds is smaller than the one used) and divide the stepsize by 10
  7. go to step 1

The resulting  $\Delta z$  is the  $z_i^+$  or  $z_i^-$ , depending on what was being calculated.

The global tolerance  $\Delta\chi^2$  can now be calculated using

$$\Delta\chi^2 = \sum_{i=1}^n \frac{(z_i^+)^2 + (z_i^-)^2}{2n}, \quad (6.12)$$

where  $n$  is the number of free parameters.

### 6.1.3. Error PDF Parameters

The error parameters, i.e. the  $n^2$  parameters for the  $2n$  error PDFs, can be calculated using

$$a_{i,j}^{\pm} = a_i^0 \pm \sqrt{\frac{\Delta\chi^2}{\lambda_j} V_i^{(j)}}, \quad (6.13)$$

where  $\{a_{1,j}^{\pm}, \dots, a_{n,j}^{\pm}\}$  are the parameters which result from varying the  $j$ th free parameter;  $a_i^0$  are the parameters for which  $\chi^2$  is minimal.

From the error parameters follow the  $2n$  error PDFs

$$f_j^{\pm} = f(\{a_{i,j}^{\pm}\}), \quad \text{for } j = 1, 2, \dots, n. \quad (6.14)$$

At this point it is worth mentioning that the  $A_G^{\text{had}}$  are calculated after the calculation of the error parameters such that the error PDFs follow the momentum sum rule.

Any observables  $X$ , which depend on the PDFs, also receive an uncertainty  $\Delta X$ . This uncertainty can be calculated using

$$\Delta X = \frac{1}{2} \sqrt{\sum_k (X(f_j^+) - X(f_j^-))^2}. \quad (6.15)$$

The error bands for the PDFs can be calculated in the same way by using

$$\Delta f = \frac{1}{2} \sqrt{\sum_k (f_j^+ - f_j^-)^2} \quad (6.16)$$

and then adding/subtracting  $\Delta f$  to/from the PDFs with the optimal free parameters. The area between these two is the so called error band.

To calculate the error bands for evolved PDFs, evolve the  $2n$  error PDFs seperately and use eq. (6.16) after that. For the structure functions, evolve the error PDFs seperately aswell and then plug them into eq. (6.15).

## 6.2. Inputs

The inputs are the same as already covered in section 5.4.

## 6.3. Results

The calculations for the error PDFs were run for Fit3, Fit4 and Fit5.

The resulting error parameters  $\{a_i^\pm\}$  can be seen in tables 5 to 7, the tolerances  $\Delta\chi^2$  can be seen in eq. (6.17).

$$\begin{aligned} \Delta\chi_{\text{Fit3LO}}^2 &= 51.5881 & \Delta\chi_{\text{Fit3HO}}^2 &= 17.6415 \\ \Delta\chi_{\text{Fit4LO}}^2 &= 14.4173 & \Delta\chi_{\text{Fit4HO}}^2 &= 9.13941 \\ \Delta\chi_{\text{Fit5LO}}^2 &= 14.2932 & \Delta\chi_{\text{Fit5HO}}^2 &= 8.65906 \end{aligned} \quad (6.17)$$

The error PDFs are shown in figs. 12 to 17.

For the high  $Q^2$  fits the comparion of LO and HO shows that down-quark PDF has its highest point for the LO at the bump at high  $x$  while the highest value at the HO is at very low  $x$ . For the up- and strange-quark the distributions seem to be weighted more to the higher  $x$  region for the LO aswell. The up-, strange- and charm-quark at LO have

a positive gradient close to  $x = 1$  whereas they have a negative gradient in this region at HO. The charm-quark PDF has, unlike the other quarks, no bump at higher  $x$ . It falls up to  $x \sim 0.1$  from where on it keeps rising.

At low  $Q^2$  values all quark PDFs start at or close to zero, rise exponentially until they reach their maximum between  $x \sim 0.1$  and  $x = 1$  after which they fall, resulting in a bump. The charm-quark PDF is zero for this  $Q^2$  value, since  $Q^2 = m_c$ .

The gluon PDF for all fits has a continuous negative slope, where the low  $Q^2$  fit is always higher than the high  $Q^2$  fit. This means that by evolving the gluon PDF it becomes smaller. It is also worth mentioning that the starting value for the gluon PDF is around one to two orders of magnitude bigger than the starting values for the quarks.

The error bands of the PDFs become very large when going to low  $x$  for the high  $Q^2$  plots and smaller for higher  $x$ . This can be especially seen for the gluon and charm-quark. At low  $Q^2$  the error bands for the quark PDFs seem to stay approximately similarly big throughout the whole  $x$  region. The behaviour of the error bands for the gluon PDFs at low  $Q^2$  is very similar to the behaviour at high  $Q^2$ .

Looking at the error parameters of Fit5 (see table 7) a problem can be seen. Some of the values for  $B_q^{\text{PL}}$  are smaller than zero, which means that the point-like contribution goes to infinity for some  $x$ -values. This results in some spikes in the error PDFs, as can be seen in figs. 16 and 17.

These spikes can also not be avoided by choosing another tolerance. For all  $B_q^{\text{PL}}$  to be positive, the maximum value for the tolerance would be  $\Delta\chi^2 \approx 1.23$ . This value is up to one order of magnitude smaller than the calculated tolerances which means that it is no good choice, because it would underestimate the inconsistency in the experimental data.

Because of this unavoidable unphysical behaviour the Fit5 input PDFs should not be considered for further discussions.

## 6. Calculation of Error PDFs

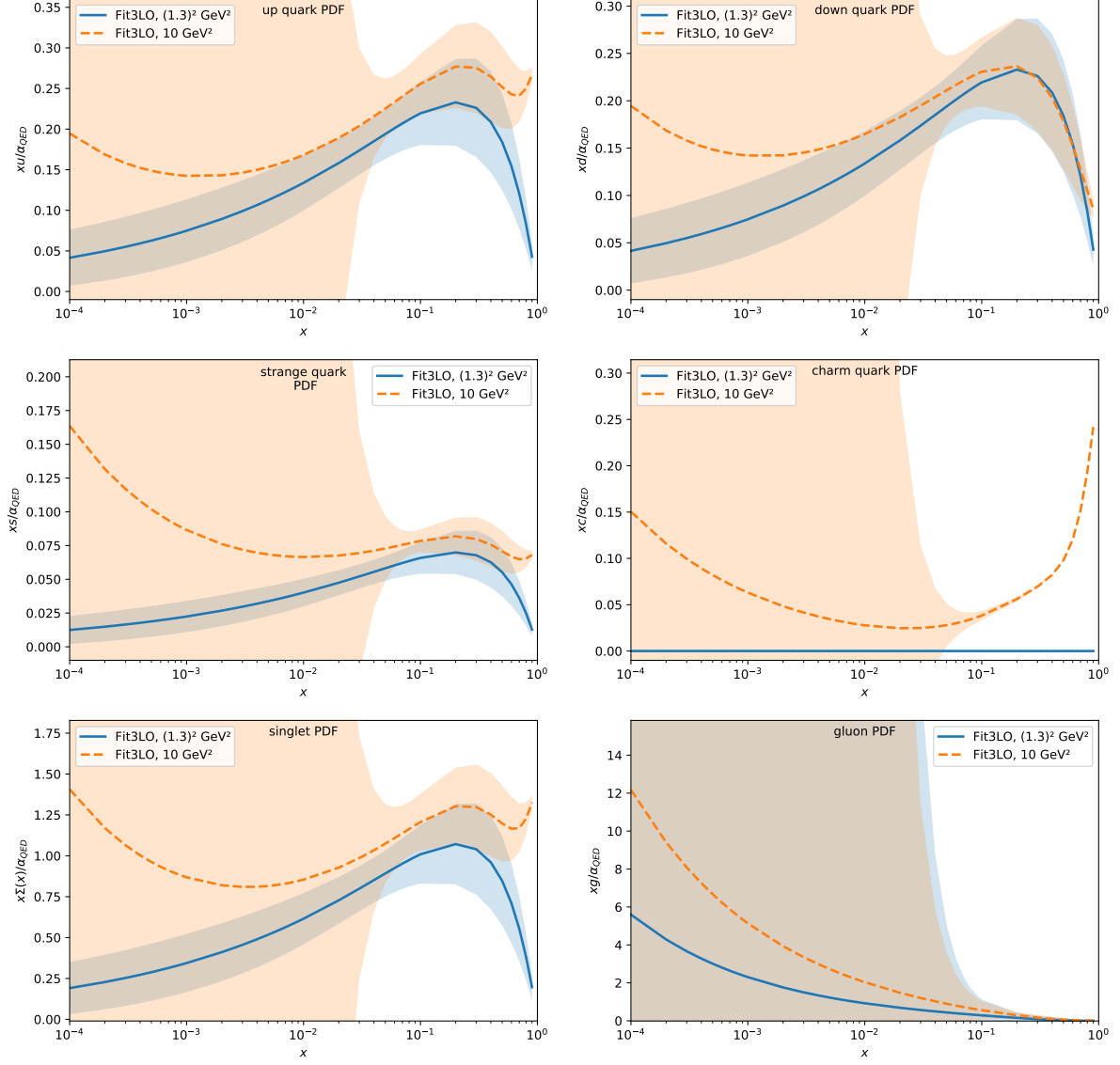


**Figure 12:** Fit3 input PDFs at LO at  $2 \text{ GeV}^2$  and  $10 \text{ GeV}^2$  including the error bands.

## 6. Calculation of Error PDFs

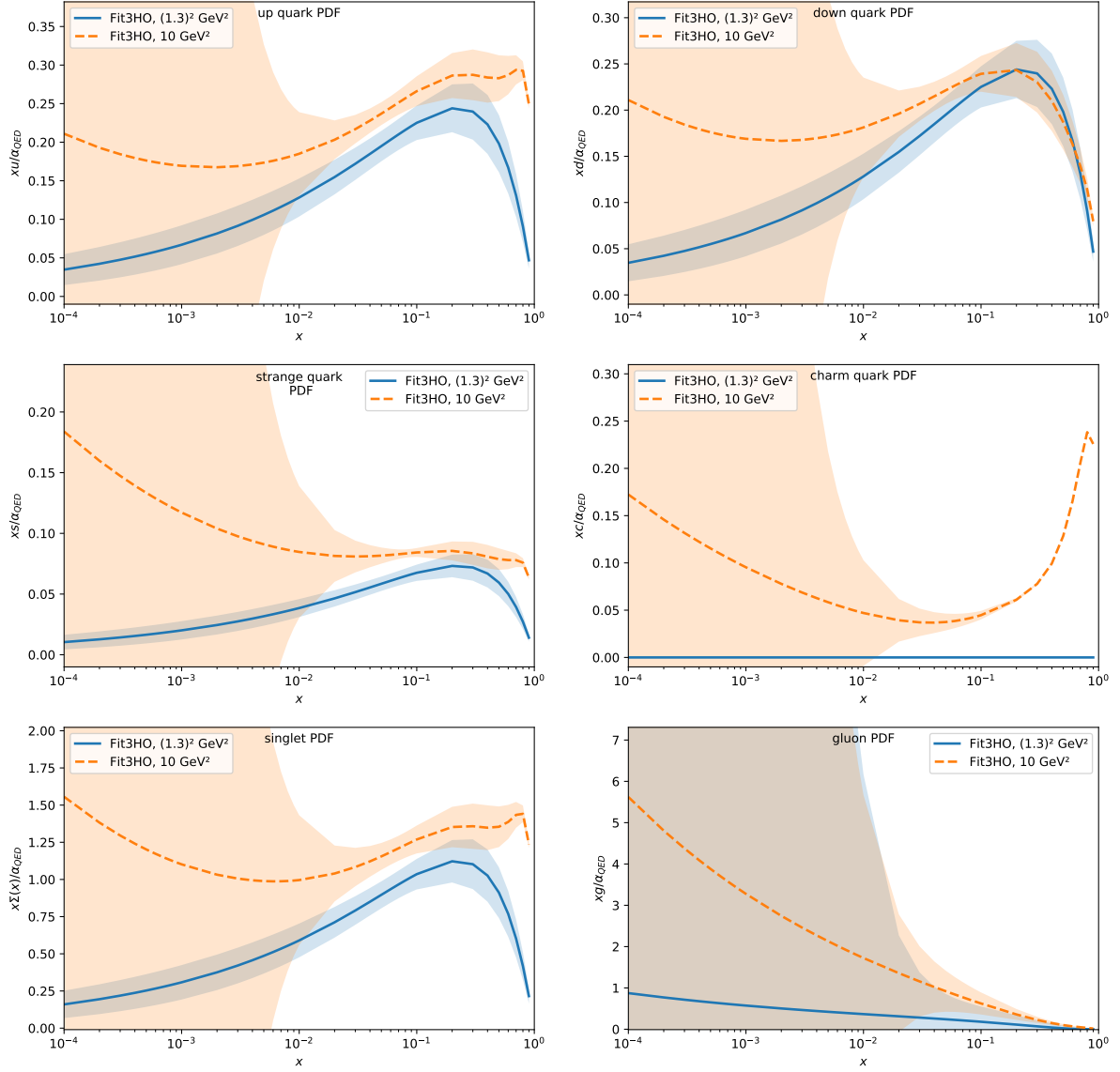


**Figure 13:** Fit3 input PDFs at HO at  $2 \text{ GeV}^2$  and  $10 \text{ GeV}^2$  including the error bands.



## 6. Calculation of Error PDFs

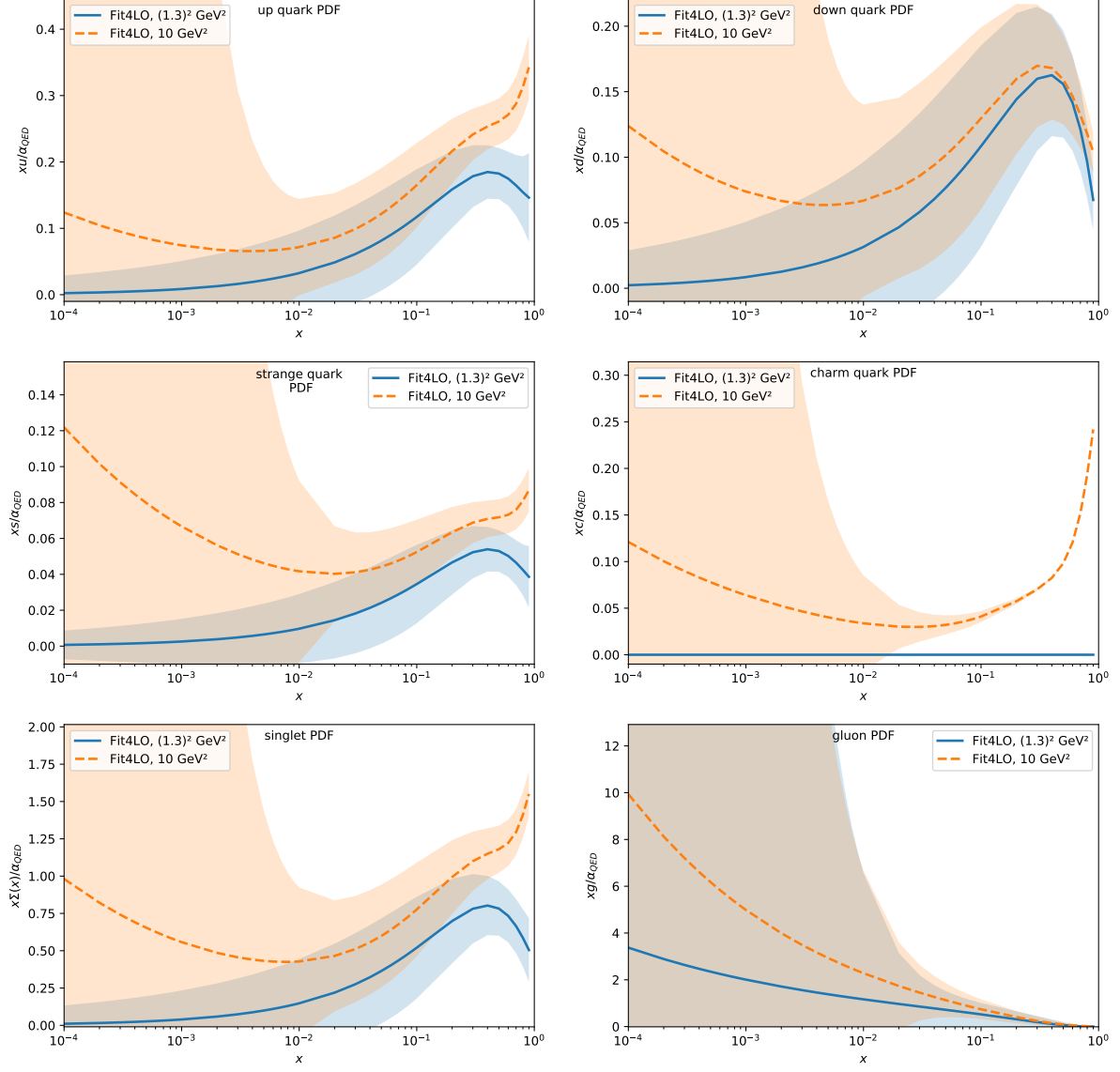


**Figure 14:** Fit4 input PDFs at LO at  $2 \text{ GeV}^2$  and  $10 \text{ GeV}^2$  including the error bands.

## 6. Calculation of Error PDFs

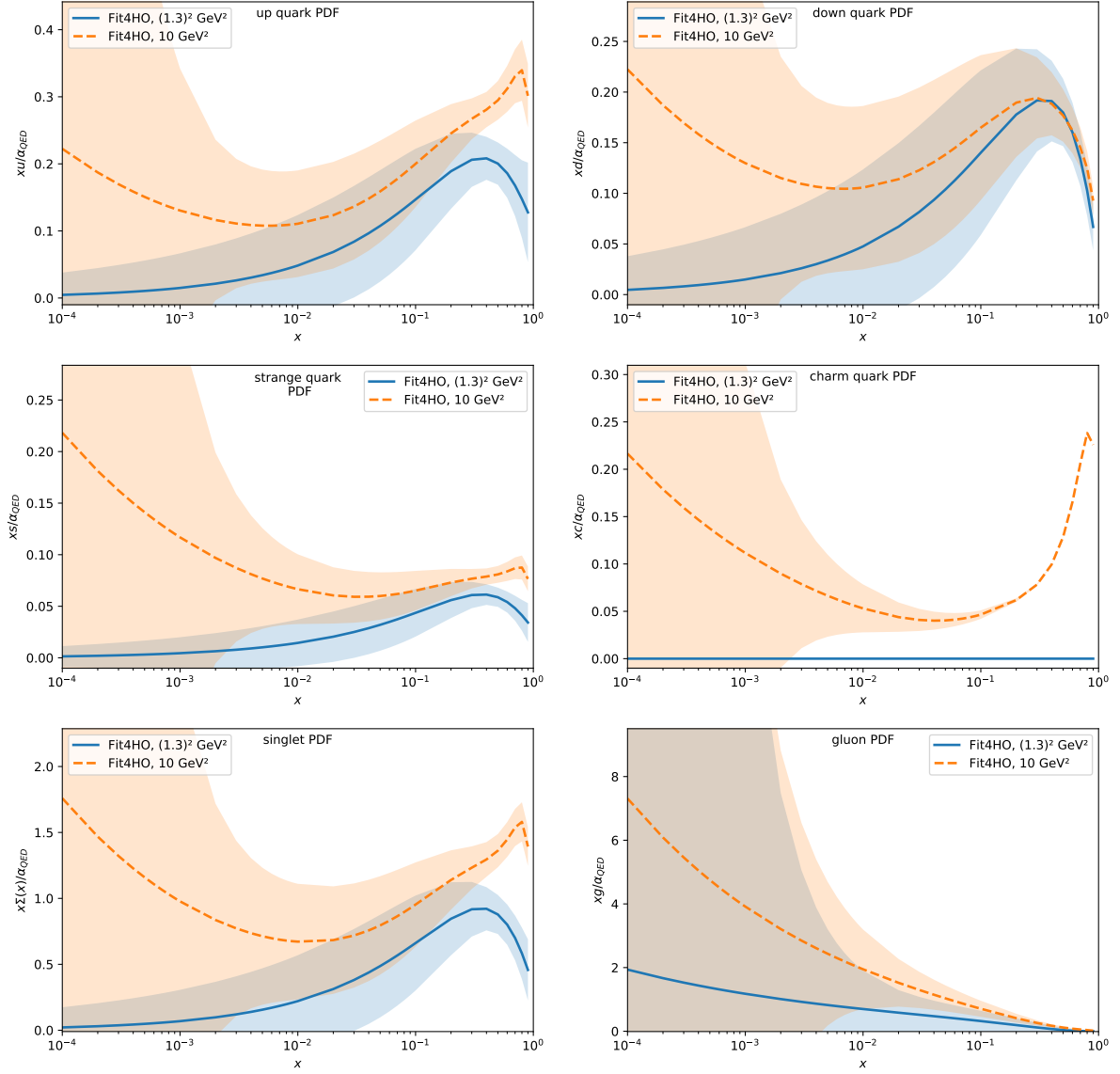


**Figure 15:** Fit4 input PDFs at HO at  $2 \text{ GeV}^2$  and  $10 \text{ GeV}^2$  including the error bands.

## 6. Calculation of Error PDFs

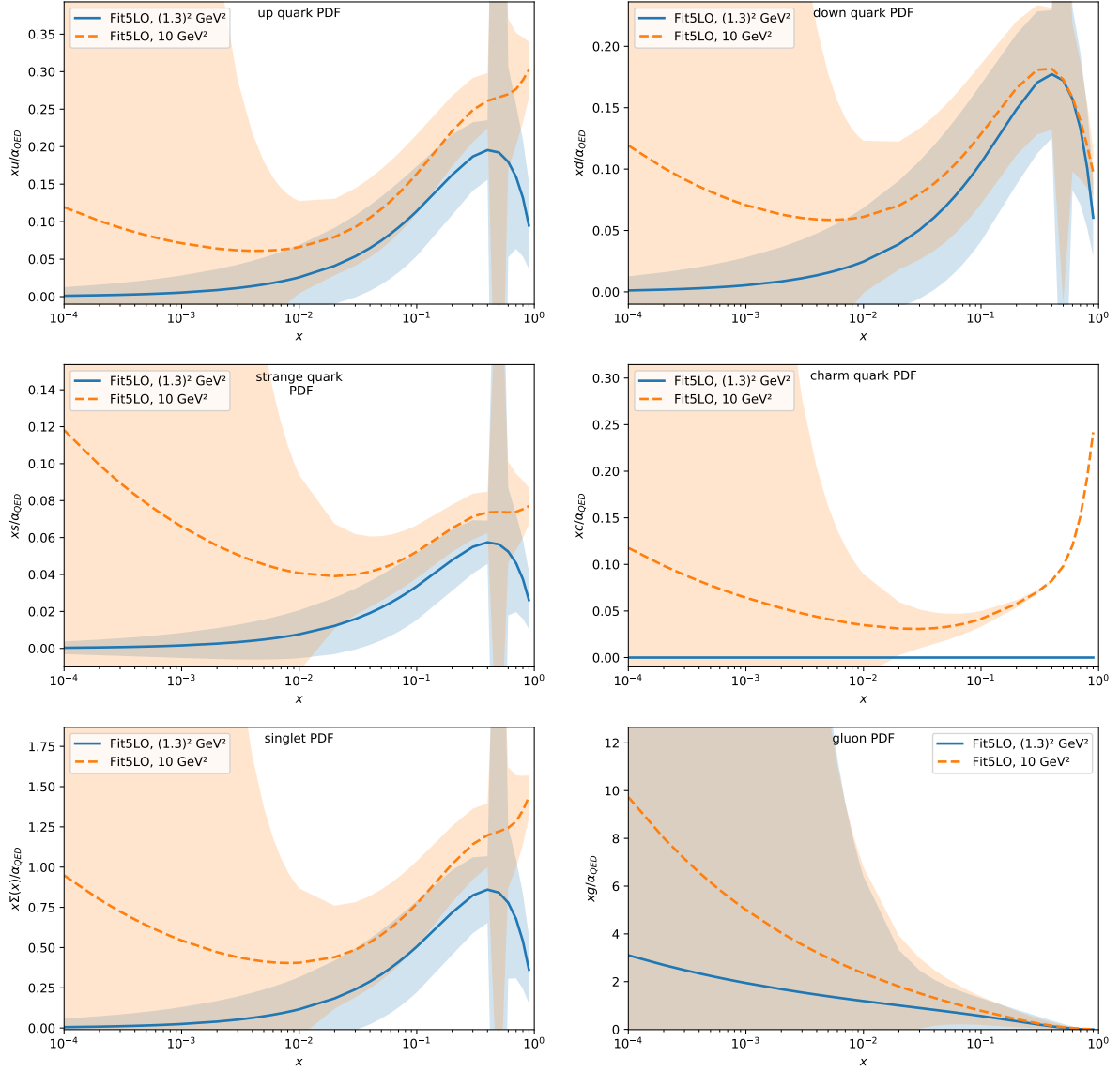


**Figure 16:** Fit5 input PDFs at LO at  $2 \text{ GeV}^2$  and  $10 \text{ GeV}^2$  including the error bands.

## 6. Calculation of Error PDFs

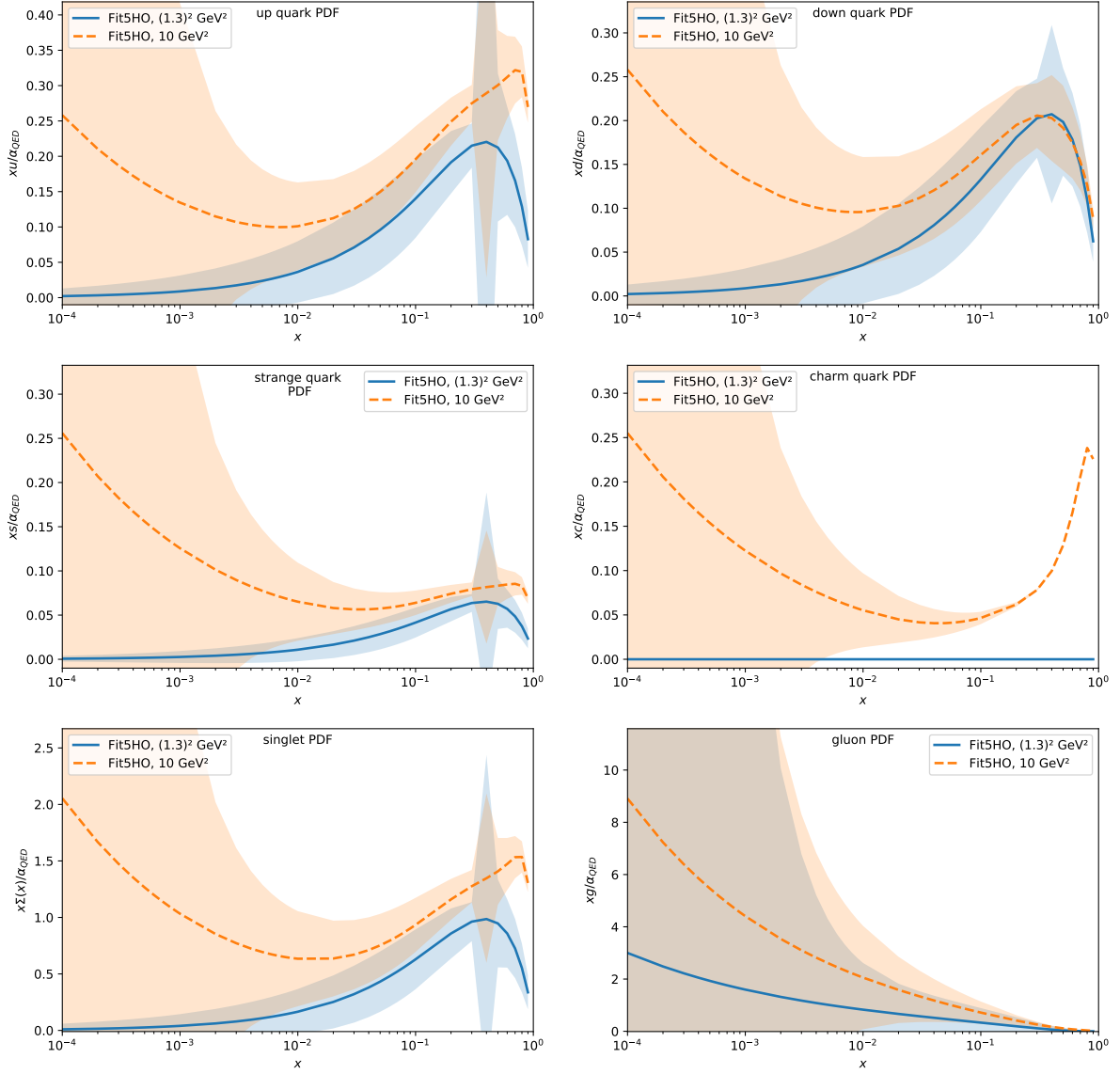


**Figure 17:** Fit5 input PDFs at HO at  $2 \text{ GeV}^2$  and  $10 \text{ GeV}^2$  including the error bands.

## 7. Comparison to measured $F_2^\gamma$ and other Photon PDFs

For illustration purposes only the results for Fit4 input PDFs will be shown here.

### 7.1. Comparison of Structure Functions

For the comparison of the calculated  $F_2^\gamma$  structure functions to experimental data, experiments from every facility (except for PEP) were chosen as an example. For LEP, ALEPH ( $9.9 \text{ GeV}^2$ ,  $20.7 \text{ GeV}^2$  and  $284 \text{ GeV}^2$ ) and OPAL ( $7.5 \text{ GeV}^2$ ,  $14.7 \text{ GeV}^2$  and  $780 \text{ GeV}^2$ ) were chosen. TRISTAN is represented by AMY ( $6.8 \text{ GeV}^2$ ,  $73 \text{ GeV}^2$  and  $390 \text{ GeV}^2$ ). PLUTO ( $2.4 \text{ GeV}^2$ ,  $4.3 \text{ GeV}^2$  and  $9.2 \text{ GeV}^2$ ) represents the PETRA facility. The experiments and  $Q^2$  values were chosen to be representative of all of the data used for the fitting.

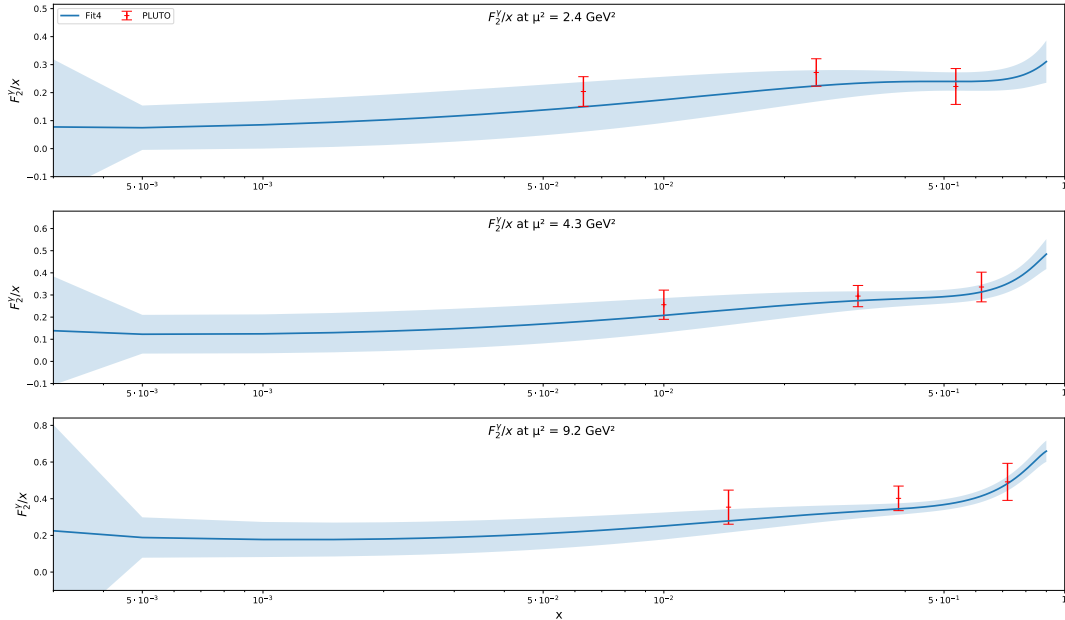


**Figure 18:** Calculated  $F_2^\gamma$  structure functions at  $2.4 \text{ GeV}^2$ ,  $4.3 \text{ GeV}^2$  and  $9.2 \text{ GeV}^2$  including their error bands compared to PLUTO experimental data at these  $Q^2$  values.

In fig. 18 it can be seen that the line for the structure function crosses the error bars of all experimental data values. This is to be expected looking at the  $\chi^2$  per degree of freedom table, table 3, as PLUTO has the lowest value there.

Looking at fig. 19 the structure functions for the lowest two shown energies seem to represent the data points in a good way aswell. Only the value with the lowest  $x$  in the first plot and two values in the last plot do not cross the calculated structure function. The one value in the first plot however is still in the error bands and the other two values

## 7. Comparison to measured $F_2^\gamma$ and other Photon PDFs

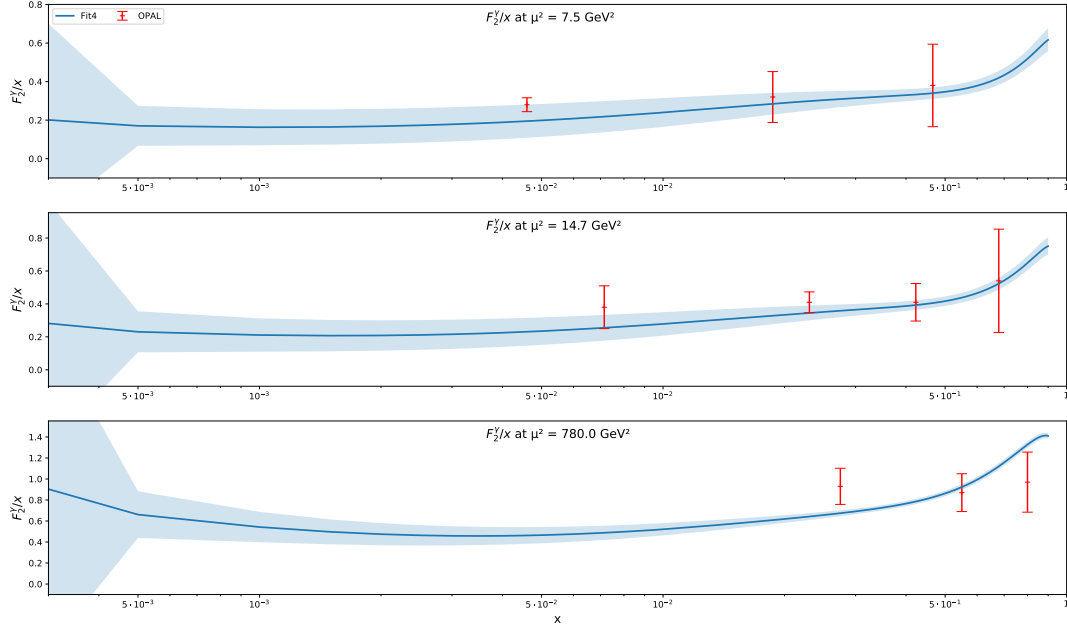


**Figure 19:** Calculated  $F_2^\gamma$  structure functions at  $7.5 \text{ GeV}^2$ ,  $14.7 \text{ GeV}^2$  and  $780 \text{ GeV}^2$  including their error bands compared to OPAL experimental data at these  $Q^2$  values.

are from the OPAL2 data set, which was only included because of its unique high  $Q^2$ . Looking at table 3 it can be seen that OPAL2 has one of the highest values, meaning it can be expected that some values from OPAL2 deviate from the calculated structure function.

The structure function seems to describe the ALEPH values quite good in fig. 20. All values except one have at least their error bars inside the error band of the structure function and more than half of these values also cross the structure function with their error bars.

For AMY three values have their error bars outside of the error band of the structure function but the structure function crosses the error bars of four values in fig. 21.

Overall the structure function and the error bands seem to represent the experimental data points quite good. One thing to note however are the very large error bands at low- $x$  values. This is due to there being very little available data points which means that the structure function is not very precise here. This could be fixed by new  $F_2^\gamma$  data for the low- $x$  region or by including dijet-data which constraints this region aswell.

## 7. Comparison to measured $F_2^\gamma$ and other Photon PDFs

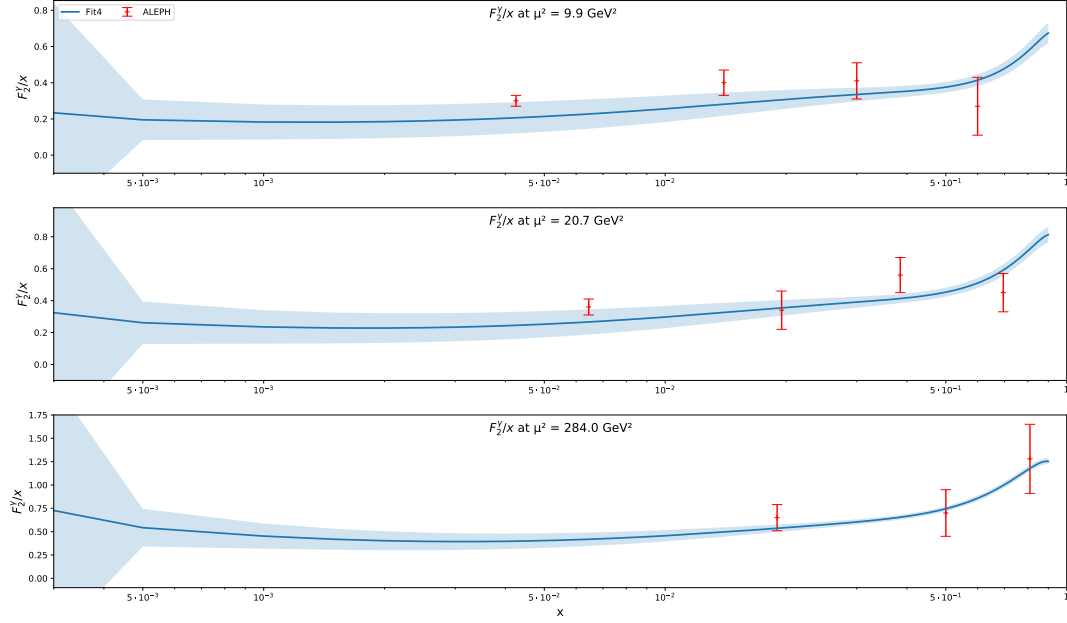


**Figure 20:** Calculated  $F_2^\gamma$  structure functions at  $9.9 \text{ GeV}^2$ ,  $20.7 \text{ GeV}^2$  and  $284 \text{ GeV}^2$  including their error bands compared to ALEPH experimental data at these  $Q^2$  values.

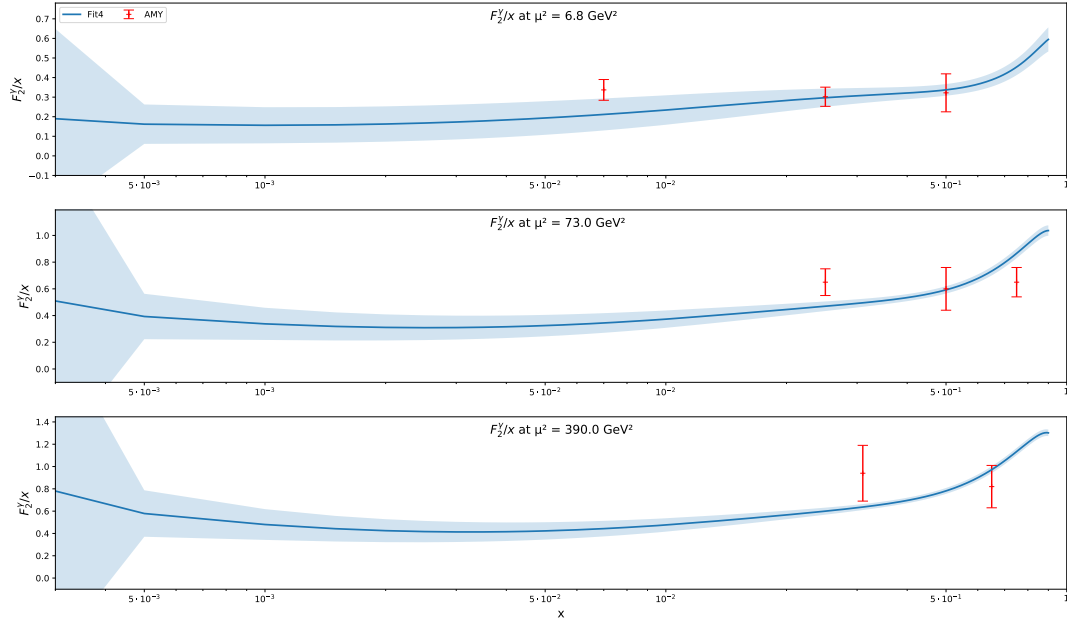


**Figure 21:** Calculated  $F_2^\gamma$  structure functions at  $6.8 \text{ GeV}^2$ ,  $73 \text{ GeV}^2$  and  $390 \text{ GeV}^2$  including their error bands compared to AMY experimental data at these  $Q^2$  values.

## 7.2. Comparison of PDFs

The SAL results for higher energies than  $2\text{ GeV}^2$  were evolved from their input PDFs using APFEL++.

The comparison to SAL [12] and GRV [16] at HO can be seen in figs. 22 and 23. Looking at the plot at a lower  $Q^2$  value, fig. 22, it can be seen, that Fit4 is, except for the strange quark, always the lowest at low- $x$ . However the uncertainty at low- $x$  is also very big. One reason for that is that there is very few  $F_2^\gamma$ -data at low- $x$ . This could be compensated up to some degree by using dijet-data, which SAL does. Another thing to note is that Fit4 seems to have, except for the up- and charm-quark, a more prominent 'bump' at higher- $x$ . Some of it might be up to a more prominent point-like contribution for Fit4 but not all of it. It is also worth mentioning that at this  $Q^2$  there is already a charm quark because of the lower mass assumed by APFEL++ in comparison to SAL and GRV.

If one goes to higher  $Q^2$  values as can be seen in fig. 23, SAL and Fit4 become very similar. For all  $x$ -values the SAL PDFs lie within the error bands of Fit4. Up to some degree this should be expected since the SAL PDFs are being evolved using the same code as used for Fit4. However even GRVHO is also very much closer to Fit4 than it was in fig. 22 and it was not evolved using APFEL++.

Comparing fig. 22 with fig. 23 it can be seen that Fit4 becomes more like SAL (at low and high  $Q^2$  values), meaning the values for low- $x$  become larger and the 'bump' at higher- $x$  becomes smaller. The SAL results and Fit4, i.e. the results produced by APFEL++, are converging when evolving to higher  $Q^2$ .

One general thing to mention is that GRV violates the momentum sum rule by exceeding it by about 49% at  $Q^2 = 2\text{ GeV}^2$ , which leads to high values for the gluons. Another difference are the used heavy quark schemes (GRV used FFNS [16]) and that GRV used less data points than were used for Fit4.

The differences to SAL could, apart from the reasons mentioned above, stem from their use of other and more data than was used here. Furthermore they used a different heavy quark scheme as well. This heavy quark scheme is more adequate for lower  $Q^2$  than the one used for the calculation of Fit4, since it is a combination of ZM-VFNS and FFNS [12].

To get more similar results to SAL and GRVHO one could use different input PDF forms, which favour higher values at low- $x$ . Furthermore the inclusion of dijet-data will certainly fix the high uncertainties at low- $x$  and will probably also lead to higher values in this region. The use of a combination of ZM-VFNS and FFNS, as done by SAL, could also lead to more accurate results in the low  $Q^2$  region.



## 7. Comparison to measured $F_2^\gamma$ and other Photon PDFs

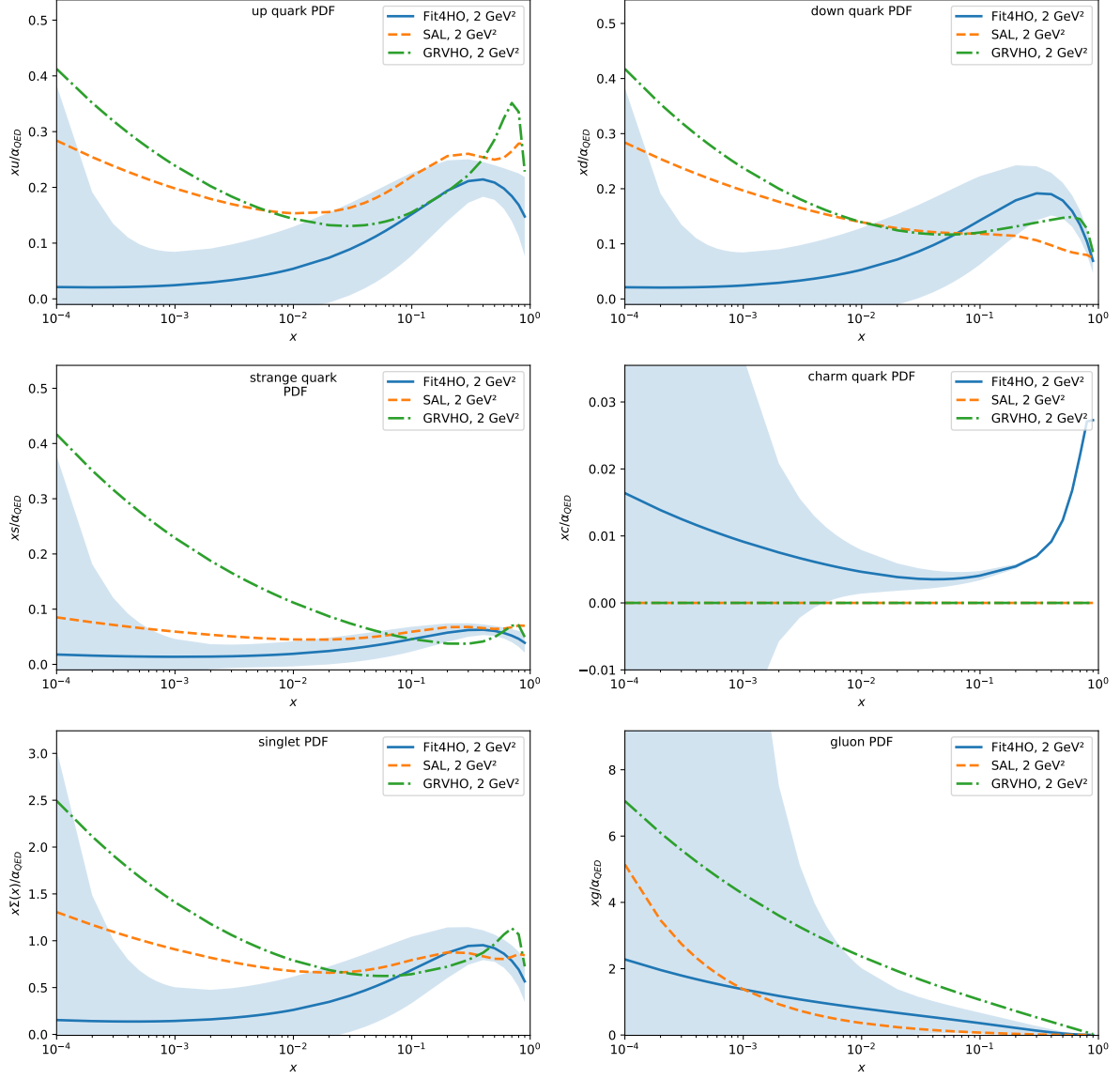


**Figure 22:** Fit4 input PDFs at HO at  $2 \text{ GeV}^2$  including the error bands, compared to SAL and GRVHO.

## 7. Comparison to measured $F_2^\gamma$ and other Photon PDFs

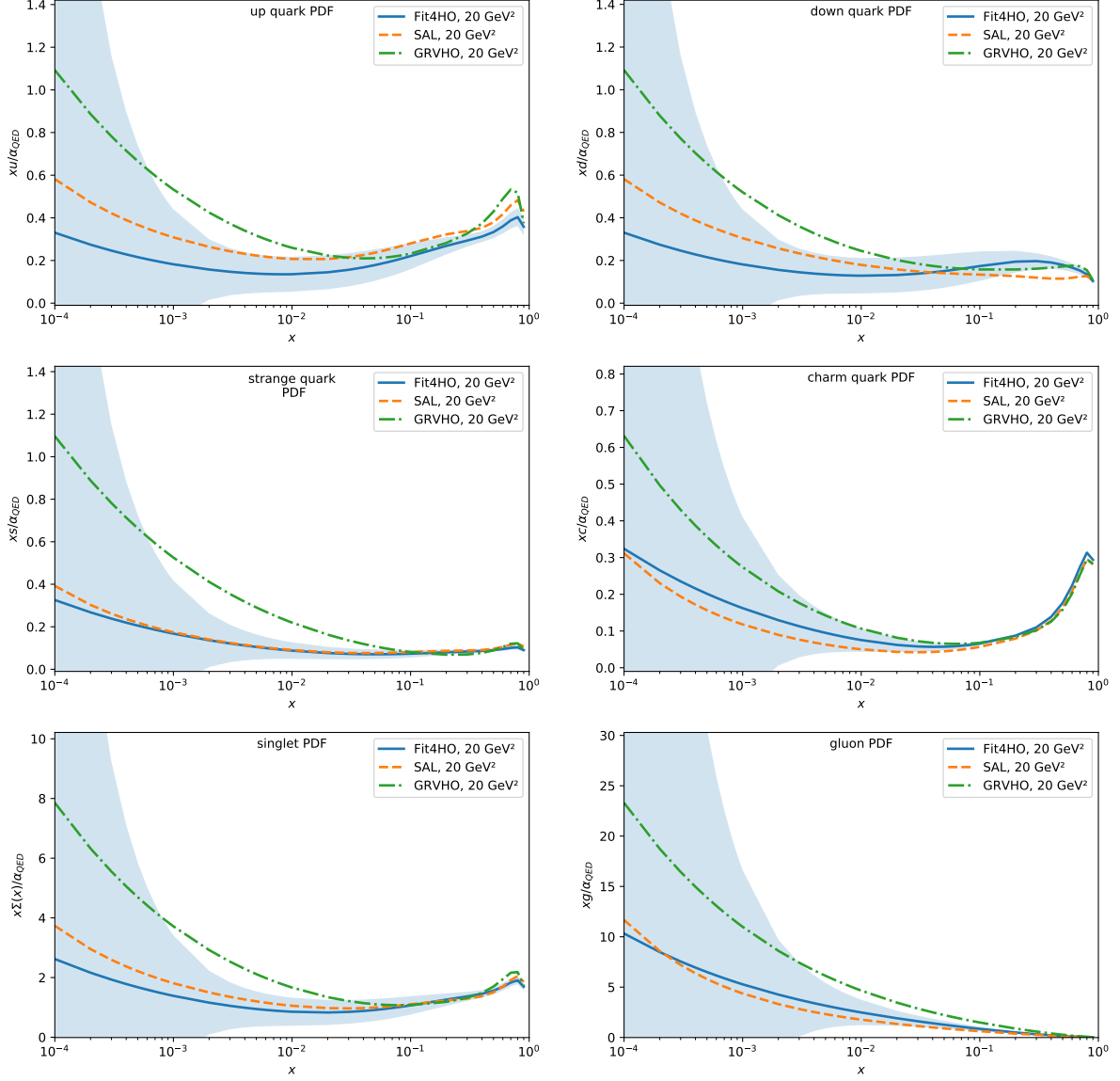


**Figure 23:** Fit4 input PDFs at HO at  $20 \text{ GeV}^2$  including the error bands, compared to SAL and GRVHO.

## 8. Conclusion and Outlook

### 8.1. Conclusion

In this thesis it was managed to implement the inhomogeneous DGLAP evolution equations into the evolution library **APFEL++**. This provides the ability to calculate photon PDFs and structure functions in a fast and modern way. The faster evolution of PDFs allows for the calculation of the uncertainties of the PDFs providing additional crucial information on the predictive power of the calculated structure functions.

Notably, despite deviations from PDFs of SAL and GRV, particularly at lower  $Q^2$  values, this serves as a robust foundation for subsequent calculations with expanded datasets and refined input PDFs. The ability to compute photon PDFs without violating the momentum sum rule and accounting for uncertainties marks a significant advancement, paving the way for more accurate predictions in the future.

### 8.2. Outlook

Due to the modern and robust foundation this work and the modified evolution library provide, it can serve as a good starting point for future advancements in the calculation of photon PDFs. Some possible changes and additions which can be done to improve on the results presented here are discussed below.

The biggest improvements can be expected from the addition of dijet data and/or future data; especially in the low  $x$  region.

As highlighted in section 3.5 adopting a heavy quark scheme that combines the fixed flavour number scheme (FFNS) and the zero-mass variable flavour number scheme (ZM-VFNS) holds promise for enhancing the results aswell.

For validating the accuracy of the calculated structure functions a comparison to experimental data not used in the fit, such as dijet data or future datasets, could be used. However, a good balance should be found as excluding data points for validation might compromise the accuracy of the fit.

The same holds for the addition of free parameters as this risks overfitting, where the calculated structure function closely mimics the fitted data and therefore lacks the predictive power for future measurements.

## A. Appendix

### A.1. Splitting Functions

The LO splitting functions are given by

$$\begin{aligned}
P_{qq}^{(0)}(x) &= C_F \left( \frac{1+x^2}{1-x} \right)_+ \\
P_{qg}^{(0)}(x) &= 2n_f T_R (x^2 + (1-x)^2) \\
P_{gq}^{(0)}(x) &= C_F \frac{1+(1-x)^2}{x} \\
P_{gg}^{(0)}(x) &= 6 \left( \frac{x}{(1-x)_+} + \frac{1-x}{x} + x(1-x) + \left( \frac{11}{12} - \frac{n_f}{18} \right) \delta(1-x) \right)
\end{aligned} \tag{A.1}$$

with  $C_F = 4/3$ ,  $T_R = 1/2$  and  $n_f$  being the number of quark flavours. They are illustrated in fig. 24.

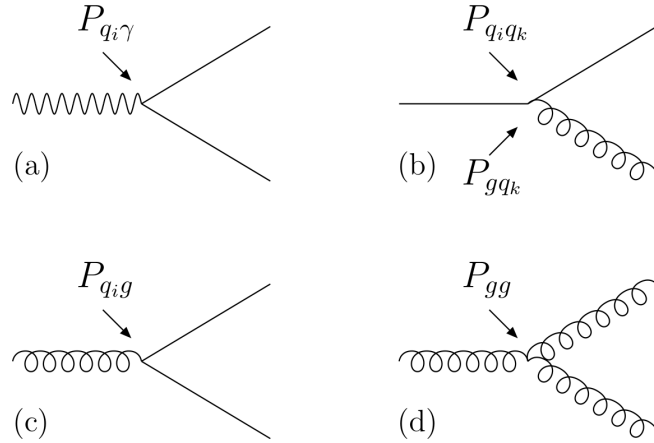


**Figure 24:** Feynman diagrams illustrating the splitting functions. Shown are (a) the branching of a photon into a quark pair, (b) the branching of a quark into a quark and a gluon, (c) the branching of a gluon into a quark pair, and (d) the branching of a gluon into two gluons.[6, Fig. B.1.]

## A.2. Input PDFs

The input PDFs used in this thesis.

**Fit3:**

$$\begin{aligned}
 \frac{1}{\alpha} x \bar{u}^\gamma(x, Q_0) &= A_q^{\text{had}} x^{B_q^{\text{had}}} (1-x) \\
 \frac{1}{\alpha} x \bar{d}^\gamma(x, Q_0) &= A_q^{\text{had}} x^{B_q^{\text{had}}} (1-x) \\
 \frac{1}{\alpha} x \bar{s}^\gamma(x, Q_0) &= 3 A_q^{\text{had}} x^{B_q^{\text{had}}} (1-x) \\
 \frac{1}{\alpha} x g^\gamma(x, Q_0) &= A_g^{\text{had}} x^{B_g^{\text{had}}} (1-x)^3.
 \end{aligned} \tag{A.2}$$

**Fit4:**

$$\begin{aligned}
 \frac{1}{\alpha} x \bar{u}^\gamma(x, Q_0) &= A_q^{\text{had}} x^{B_q^{\text{had}}} (1-x) + A_q^{\text{PL}} e_u^2 x (x^2 + (1-x)^2) \\
 \frac{1}{\alpha} x \bar{d}^\gamma(x, Q_0) &= A_q^{\text{had}} x^{B_q^{\text{had}}} (1-x) + A_q^{\text{PL}} e_d^2 x (x^2 + (1-x)^2) \\
 \frac{1}{\alpha} x \bar{s}^\gamma(x, Q_0) &= 3 A_q^{\text{had}} x^{B_q^{\text{had}}} (1-x) + A_q^{\text{PL}} e_s^2 x (x^2 + (1-x)^2) \\
 \frac{1}{\alpha} x g^\gamma(x, Q_0) &= A_g^{\text{had}} x^{B_g^{\text{had}}} (1-x)^3.
 \end{aligned} \tag{A.3}$$

**Fit5:**

$$\begin{aligned}
 \frac{1}{\alpha} x \bar{u}^\gamma(x, Q_0) &= A_q^{\text{had}} x^{B_q^{\text{had}}} (1-x) + A_q^{\text{PL}} e_u^2 x \frac{x^2 + (1-x)^2}{1 - B_q^{\text{PL}} \ln(1-x)} \\
 \frac{1}{\alpha} x \bar{d}^\gamma(x, Q_0) &= A_q^{\text{had}} x^{B_q^{\text{had}}} (1-x) + A_q^{\text{PL}} e_d^2 x \frac{x^2 + (1-x)^2}{1 - B_q^{\text{PL}} \ln(1-x)} \\
 \frac{1}{\alpha} x \bar{s}^\gamma(x, Q_0) &= 3 A_q^{\text{had}} x^{B_q^{\text{had}}} (1-x) + A_q^{\text{PL}} e_s^2 x \frac{x^2 + (1-x)^2}{1 - B_q^{\text{PL}} \ln(1-x)} \\
 \frac{1}{\alpha} x g^\gamma(x, Q_0) &= A_g^{\text{had}} x^{B_g^{\text{had}}} (1-x)^3.
 \end{aligned} \tag{A.4}$$

### A.3. $\chi^2$ Values

**Table 4:** Global  $\chi^2$  and  $\chi^2$  for each experiment for the calculated initial parameters given in table 2.

	Fit3		Fit4		Fit5	
	LO	HO	LO	HO	LO	HO
$\chi^2$	129.127	122.271	113.702	116.328	109.416	111.309
<b>ALEPH1</b>	4.631999	4.693253	5.243729	5.449274	4.951805	5.276600
<b>ALEPH2</b>	15.418790	14.289682	12.980662	13.652734	11.979753	12.628888
<b>AMY</b>	5.954416	8.016832	7.231337	9.677344	6.755615	9.153060
<b>DELPHI</b>	2.690830	3.537173	2.649599	3.533339	2.609416	3.486373
<b>JADE</b>	12.668449	16.236593	15.005252	18.604377	13.949602	17.740634
<b>L3</b>	31.183795	20.721322	22.266086	13.795326	21.660302	13.202273
<b>OPAL1</b>	13.186186	12.184885	10.328188	10.317035	9.978544	9.780750
<b>OPAL2</b>	8.601775	11.383352	8.545542	11.430371	8.038476	10.956999
<b>PLUTO</b>	12.179568	7.556982	7.056111	5.820943	7.757468	5.829135
<b>TASSO</b>	7.354201	7.859130	6.684778	7.840202	6.382201	7.309615
<b>TOPAZ</b>	15.257284	15.791789	15.711129	16.207289	15.353038	15.944428

### A.4. Error Parameters

**Table 5:** Error parameters calculated for the Fit3 initial PDFs with a tolerance of  $\Delta\chi^2 = 51.5881$  for LO and  $\Delta\chi^2 = 17.6415$  for HO.

Fit3		$A_q^{\text{had}}$	$B_q^{\text{had}}$	$A_q^{\text{PL}}$	$B_q^{\text{PL}}$	$A_q^{\text{had}}$	$B_q^{\text{had}}$
LO	$\{a_i^-\}$	0.410966	0.241663			6.162709	1.701252
		0.415975	0.289040			0.264201	-0.384680
		0.613191	0.382083			-0.062629	-0.381306
	$\{a_i^-\}$	0.468584	0.270819			0.006560	-2.470414
		0.463575	0.223442			0.052119	-0.384482
		0.266359	0.130399			0.478590	-0.387856
HO	$\{a_i^+\}$	0.471788	0.263275			-0.008044	-1.584507
		0.497361	0.265353			0.050702	-0.182259
		0.597581	0.365750			-0.089042	-0.184680
	$\{a_i^-\}$	0.494360	0.308351			1.684169	1.219561
		0.468787	0.306273			0.269892	-0.182687
		0.368567	0.205876			0.481466	-0.180266

**Table 6:** Error parameters calculated for the Fit4 initial PDFs with a tolerance of  $\Delta\chi^2 = 14.4173$  for LO and  $\Delta\chi^2 = 9.13941$  for HO.

Fit4		$A_q^{\text{had}}$	$B_q^{\text{had}}$	$A_q^{\text{PL}}$	$B_q^{\text{PL}}$	$A_q^{\text{had}}$	$B_q^{\text{had}}$
LO	$\{a_i^+\}$	0.423601	0.587038	0.293050	0.0	0.510566	-0.224523
		0.419789	0.646472	0.369970	0.0	3.637302	0.891686
		0.554525	0.567427	0.263078	0.0	0.161463	-0.219911
		0.532487	0.940363	0.493398	0.0	0.374764	-0.255715
	$\{a_i^-\}$	0.449305	0.554704	0.347886	0.0	0.342019	-0.224381
		0.453117	0.495270	0.270966	0.0	-0.022813	-1.340590
		0.318381	0.574315	0.377858	0.0	0.684556	-0.228993
		0.340419	0.201379	0.147538	0.0	0.414053	-0.193189
HO	$\{a_i^+\}$	0.501738	0.492109	0.264223	0.0	0.194853	-0.214520
		0.477027	0.526221	0.299600	0.0	-0.011561	-1.129076
		0.392882	0.496229	0.300003	0.0	0.497476	-0.210690
		0.569403	0.813966	0.447821	0.0	0.269517	-0.197890
	$\{a_i^-\}$	0.480646	0.519731	0.230125	0.0	0.338076	-0.215536
		0.505357	0.485619	0.194748	0.0	1.342914	0.699020
		0.589502	0.515611	0.194345	0.0	0.047642	-0.219366
		0.412981	0.197874	0.046527	0.0	0.176783	-0.232166

**Table 7:** Error parameters calculated for the Fit5 initial PDFs with a tolerance of  $\Delta\chi^2 = 14.2932$  for LO and  $\Delta\chi^2 = 8.65906$  for HO.

Fit5		$A_q^{\text{had}}$	$B_q^{\text{had}}$	$A_q^{\text{PL}}$	$B_q^{\text{PL}}$	$A_q^{\text{had}}$	$B_q^{\text{had}}$
LO	$\{a_i^+\}$	0.535753	0.648331	0.379272	0.647915	0.411621	-0.202163
		0.418741	0.693203	0.401024	0.655961	0.752809	-0.206463
		0.525042	0.750064	0.392915	0.647863	3.917671	0.905852
		0.691142	1.031506	0.489169	0.623470	0.426054	-0.235978
		0.696122	0.726785	0.359916	2.760467	0.243766	-0.206259
	$\{a_i^-\}$	0.514153	0.681899	0.317570	0.649021	0.551227	-0.202257
		0.631165	0.637027	0.295818	0.640975	0.189035	-0.197957
		0.524864	0.580166	0.303927	0.649073	-0.024714	-1.310272
		0.358764	0.298724	0.207673	0.673466	0.593631	-0.168442
		0.353784	0.603445	0.336926	-1.463531	1.209678	-0.198161
HO	$\{a_i^+\}$	0.601786	0.595853	0.316540	1.115821	0.191225	-0.272153
		0.672186	0.593869	0.243075	1.113081	0.049973	-0.276829
		0.579399	0.556545	0.230116	1.135448	1.208965	0.603607
		0.747812	0.896306	0.437117	1.109835	0.250495	-0.242100
		0.706345	0.619386	0.300060	4.079597	0.045660	-0.335672
	$\{a_i^-\}$	0.581964	0.625907	0.277684	1.116509	0.293530	-0.273557
		0.511564	0.627891	0.351149	1.119249	0.433116	-0.268881
		0.604351	0.665215	0.364108	1.096882	-0.013635	-1.149317
		0.435938	0.325454	0.157107	1.122495	0.269378	-0.303610
		0.477405	0.602374	0.294164	-1.847267	0.826358	-0.210038

## References

- [1] Valerio Bertone, Stefano Carrazza, and Juan Rojo. “APFEL: A PDF evolution library with QED corrections”. In: *Computer Physics Communications* 185.6 (June 2014), pp. 1647–1668. ISSN: 0010-4655. DOI: 10.1016/j.cpc.2014.03.007. URL: <http://dx.doi.org/10.1016/j.cpc.2014.03.007>.
- [2] Valerio Bertone. *APFEL++: A new PDF evolution library in C++*. 2017. arXiv: 1708.00911 [hep-ph].
- [3] Vadim Guzey. *Notes on photon PDFs*. vadim.a.guzey@jyu.fi. 2022.
- [4] Hannu Paukkunen. *Global analysis of nuclear parton distribution functions at leading and next-to-leading order perturbative QCD*. 2009. arXiv: 0906.2529 [hep-ph].
- [5] Francis Halzen and Alan D. Martin. *QUARKS & LEPTONS: An Introductory Course In Modern Particle Physics*. 1984. ISBN: 978-8-126-51656-8.
- [6] Richard Nisius. “The photon structure from deep inelastic electron–photon scattering”. In: *Physics Reports* 332.4–6 (July 2000), pp. 165–317. ISSN: 0370-1573. DOI: 10.1016/S0370-1573(99)00115-5. URL: [http://dx.doi.org/10.1016/S0370-1573\(99\)00115-5](http://dx.doi.org/10.1016/S0370-1573(99)00115-5).
- [7] M. Glück and E. Reya. “Boundary conditions for the photon structure function in the leading and subleading order”. In: *Phys. Rev. D* 28 (11 Dec. 1983), pp. 2749–2755. DOI: 10.1103/PhysRevD.28.2749. URL: <https://link.aps.org/doi/10.1103/PhysRevD.28.2749>.
- [8] M. Glück, E. Reya, and A. Vogt. “Parton structure of the photon beyond the leading order”. In: *Phys. Rev. D* 45 (11 June 1992), pp. 3986–3994. DOI: 10.1103/PhysRevD.45.3986. URL: <https://link.aps.org/doi/10.1103/PhysRevD.45.3986>.
- [9] Andreas Vogt. *The Parton Structure of Real Photons*. 1997. arXiv: hep-ph/9709345 [hep-ph].
- [10] John C. Collins, Davison E. Soper, and George Sterman. *Factorization of Hard Processes in QCD*. 2004. arXiv: hep-ph/0409313 [hep-ph].
- [11] George Sterman et al. “Handbook of perturbative QCD”. In: *Rev. Mod. Phys.* 67 (1 Jan. 1995), pp. 157–248. DOI: 10.1103/RevModPhys.67.157. URL: <https://link.aps.org/doi/10.1103/RevModPhys.67.157>.
- [12] W. Slominski, H. Abramowicz, and A. Levy. “NLO photon parton parametrization using ee and ep data”. In: *The European Physical Journal C* 45.3 (Jan. 2006). DOI: 10.1140/epjc/s2005-02458-7. URL: <https://doi.org/10.1140/epjc/s2005-02458-7>.



- [13] Valerio Bertone. *GitHub: vbertone/apfelxx: A PDF evolution library in C++*. URL: <https://github.com/vbertone/apfel>.
- [14] Valerio Bertone. *GitHub: vbertone/APFEL-Examples*. URL: <https://github.com/vbertone/APFEL-Examples>.
- [15] Alexander Epping. *GitHub: alexanderepping/apfelxx\_photon\_mod: Modification of the vbertone/apfelxx code to allow the calculation of photon PDFs*. URL: [https://github.com/alexanderepping/apfelxx\\_photon\\_mod](https://github.com/alexanderepping/apfelxx_photon_mod).
- [16] M. Glück, E. Reya, and A. Vogt. “Photonic parton distributions”. In: *Phys. Rev. D* 46 (5 Sept. 1992), pp. 1973–1979. DOI: 10.1103/PhysRevD.46.1973. URL: <https://link.aps.org/doi/10.1103/PhysRevD.46.1973>.
- [17] K. Kovarik et al. “nCTEQ15: Global analysis of nuclear parton distributions with uncertainties in the CTEQ framework”. In: *Phys. Rev. D* 93 (8 Apr. 2016), p. 085037. DOI: 10.1103/PhysRevD.93.085037. URL: <https://link.aps.org/doi/10.1103/PhysRevD.93.085037>.
- [18] Doug Hague. *GitHub: doughague/minuit-cpp: C++ Minimization Package*. URL: <https://github.com/doughague/minuit-cpp>.
- [19] R. Barate et al. “Measurement of the hadronic photon structure function at LEP-1 for  $(Q^2)$  values between 9.9-GeV<sup>2</sup> and 284-GeV<sup>2</sup>”. In: *Phys. Lett. B* 458 (1999), pp. 152–166. DOI: 10.1016/S0370-2693(99)00559-6.
- [20] A. Heister et al. “Measurement of the hadronic photon structure function  $F_2(\gamma)(x, Q^2)$  in two-photon collisions at LEP”. In: *Eur. Phys. J. C* 30 (2003), pp. 145–158. DOI: 10.1140/epjc/s2003-01291-4.
- [21] P. Abreu et al. “A Measurement of the photon structure function  $F_2(\gamma)$  at an average  $Q^2$  of 12-GeV<sup>2</sup>/c<sup>4</sup>”. In: *Z. Phys. C* 69 (1996), pp. 223–234. DOI: 10.1007/s002880050022.
- [22] M. Acciarri et al. “Study of the hadronic photon structure function  $F_2(\gamma)$  at LEP”. In: *Phys. Lett. B* 436 (1998), pp. 403–416. DOI: 10.1016/S0370-2693(98)01025-9.
- [23] M. Acciarri et al. “The  $Q^2$  evolution of the hadronic photon structure function  $F_2(\gamma)$  at LEP”. In: *Phys. Lett. B* 447 (1999), pp. 147–156. DOI: 10.1016/S0370-2693(98)01552-4.
- [24] K. Ackerstaff et al. “Analysis of hadronic final states and the photon structure function  $F_2(\gamma)$  in deep inelastic electron - photon scattering at LEP”. In: *Z. Phys. C* 74 (1997), pp. 33–48. DOI: 10.1007/s002880050368.
- [25] K. Ackerstaff et al. “Measurement of the  $Q^2$  evolution of the photon structure function  $F_2(\gamma)$ ”. In: *Phys. Lett. B* 411 (1997), pp. 387–401. DOI: 10.1016/S0370-2693(97)01023-X. arXiv: hep-ex/9708019.

- [26] K. Ackerstaff et al. “Measurement of the photon structure function  $F_2^{\gamma}$  at low  $x$ ”. In: *Phys. Lett. B* 412 (1997), pp. 225–234. DOI: 10.1016/S0370-2693(97)01022-8. arXiv: hep-ex/9708028.
- [27] R. Akers et al. “Measurement of the photon structure function  $F_2(\gamma)$  in the reaction  $e^+e^- \rightarrow e^+e^- + \text{hadrons}$  at LEP”. In: *Z. Phys. C* 61 (1994), pp. 199–208. DOI: 10.1007/BF01413097.
- [28] G. Abbiendi et al. “Measurement of the low  $x$  behavior of the photon structure function  $F_2^{\gamma}$ ”. In: *Eur. Phys. J. C* 18 (2000), pp. 15–39. DOI: 10.1007/s100520000523. arXiv: hep-ex/0007018.
- [29] G. Abbiendi et al. “Measurement of the hadronic photon structure function  $F_2^{\gamma}(2)$  at LEP-2”. In: *Phys. Lett. B* 533 (2002), pp. 207–222. DOI: 10.1016/S0370-2693(02)01560-5. arXiv: hep-ex/0202035.
- [30] T. Sasaki et al. “A Measurement of the photon structure function  $F_2$ ”. In: *Phys. Lett. B* 252 (1990), pp. 491–498. DOI: 10.1016/0370-2693(90)90577-S.
- [31] S. K. Sahu et al. “A High  $Q^2$  measurement of the photon structure function  $F_2^{\gamma}$ ”. In: *Phys. Lett. B* 346 (1995). Ed. by H. Sagawa et al., pp. 208–216. DOI: 10.1016/0370-2693(95)00092-Y.
- [32] T. Kojima et al. “A Measurement of the photon structure function  $F_2(\gamma)$  at  $Q^2 = 6.8\text{-GeV}^2$ ”. In: *Phys. Lett. B* 400 (1997), pp. 395–400. DOI: 10.1016/S0370-2693(97)00349-3.
- [33] K. Muramatsu et al. “Measurement of the photon structure function  $F_2^{\gamma}$  and jet production at TRISTAN”. In: *Phys. Lett. B* 332 (1994), pp. 477–487. DOI: 10.1016/0370-2693(94)91284-X.
- [34] W. Bartel et al. “Experimental Study of the Photon Structure Function  $F_2$  at  $Q^2$  from  $10\text{-GeV}^2$  to  $220\text{-GeV}^2$ ”. In: *Z. Phys. C* 24 (1984), p. 231.
- [35] Christoph Berger et al. “Measurement of the Photon Structure Function  $F_2(x, Q^2)$ ”. In: *Phys. Lett. B* 142 (1984), pp. 111–118. DOI: 10.1016/0370-2693(84)91145-6.
- [36] Christoph Berger et al. “Measurement and QCD Analysis of the Photon Structure Function  $F_2(x, Q^2)$ ”. In: *Nucl. Phys. B* 281 (1987). Ed. by S. C. Loken, p. 365. DOI: 10.1016/0550-3213(87)90410-X.
- [37] M. Althoff et al. “Measurement of the Photon Structure Function  $f_2^{\gamma}$  at  $Q^2$  from  $7\text{-GeV}/c^2$  to  $70\text{-GeV}/c^2$ ”. In: *Z. Phys. C* 31 (1986), p. 527. DOI: 10.1007/BF01551073.
- [38] H. Aihara et al. “Measurement of the photon structure function  $F_2^{\gamma}(x, Q^2)$  in the region  $0.2 < Q^2 < 7 \text{ GeV}^2$ ”. In: *Z. Phys. C* 34 (1987). Ed. by S. C. Loken, p. 1. DOI: 10.1007/BF01561108.

- [39] W. Slominski, H. Abramowicz, and A. Levy. “NLO photon parton parametrization using ee and ep data”. In: *Eur. Phys. J. C* 45 (2006), pp. 633–641. DOI: 10.1140/epjc/s2005-02458-7. arXiv: hep-ph/0504003.
- [40] Simon Albino, Michael Klasen, and Stefan Söldner-Rembold. “Strong Coupling Constant from the Photon Structure Function”. In: *Physical Review Letters* 89.12 (Aug. 2002). DOI: 10.1103/physrevlett.89.122004. URL: <https://doi.org/10.1103/physrevlett.89.122004>.
- [41] K.J Eskola, H Paukkunen, and C.A Salgado. “EPS09 — A new generation of NLO and LO nuclear parton distribution functions”. In: *Journal of High Energy Physics* 2009.04 (Apr. 2009), pp. 065–065. DOI: 10.1088/1126-6708/2009/04/065. URL: <https://doi.org/10.1088/1126-6708/2009/04/065>.

## **Acknowledgments**

Firstly, I would like to thank Prof. Dr. Michael Klasen for giving me the possibility to write my Master's thesis in his group, the opportunity to collaborate with a researcher from another university and country, and the experience I gained from that.

I would also like to thank Vadim Guzey for the endless explanations, input, guidance, and patience.

Next, I would like to thank Niklas H. W. Humberg, Carlson Büth, and Giulia Egbring for the great time and the friendship we had during our time in university.

Furthermore, I want to thank Klara Behrendt for her friendship and for always having an open ear for me, especially when times were not easy.

A special thanks goes to my family Angelika, Marcus and Katharina Epping for their constant support and guidance.

Last but not least, I want to thank my girlfriend Leonie Siebert. Thank you for your never-ending support and for always being there for me.

## **Declaration of Academic Integrity**

I hereby confirm that this thesis, entitled “*Global determination of parton distribution functions in the real photon at next-to-leading order in QCD including uncertainties*” is solely my own work and that I have used no sources or aids other than the ones stated. All passages in my thesis for which other sources, including electronic media, have been used, be it direct quotes or content references, have been acknowledged as such and the sources cited. I am aware that plagiarism is considered an act of deception which can result in sanction in accordance with the examination regulations.

---

(date, signature of student)

I consent to having my thesis cross-checked with other texts to identify possible similarities and to having it stored in a database for this purpose.

I confirm that I have not submitted the following thesis in part or while as an examination paper before.

---

(date, signature of student)